

A comprehensive analysis of the hard X-ray spectra of bright Seyfert galaxies^{*}

P. Lubinski^{1†}, V. Beckmann², L. Gibaud^{3‡}, S. Paltani³, I. E. Papadakis^{4,5}, C. Ricci⁶, S. Soldi², M. Türlér³, R. Walter³, A. A. Zdziarski⁷

¹*Institute of Physics, University of Zielona Góra, Licealna 9, PL-65-417 Zielona Góra, Poland*

²*François Arago Centre, APC, Université Paris Diderot, CNRS/IN2P3, CEA/Irfu, Observatoire de Paris, 13 rue Watt, 75013 Paris, France*

³*Department of Astronomy, University of Geneva, Chemin d'Ecogia 16, CH-1290 Versoix, Switzerland*

⁴*Physics Department, University of Crete, PO Box 2208, 710 03 Heraklion, Crete, Greece*

⁵*IESL, Foundation for Research and Technology, 711 10, Heraklion, Crete, Greece*

⁶*Pontificia Universidad Católica de Chile, Instituto de Astrofísica, Casilla 306, Santiago 22, Chile; EMBIGGEN Anillo, Concepción, Chile*

⁷*Centrum Astronomiczne im. M. Kopernika, Bartyczna 18, PL-00-716 Warszawa, Poland*

Accepted XXX. Received YYY; in original form ZZZ

ABSTRACT

Hard X-ray spectra of 28 bright Seyfert galaxies observed with *INTEGRAL* were analyzed together with the X-ray spectra from *XMM-Newton*, *Suzaku* and *RXTE*. These broad-band data were fitted with a model assuming a thermal Comptonization as a primary continuum component. We tested several model options through a fitting of the Comptonized continuum accompanied by a complex absorption and a Compton reflection. Both the large data set used and the model space explored allowed us to accurately determine a mean temperature kT_e of the electron plasma, the Compton parameter y and the Compton reflection strength R for the majority of objects in the sample. Our main finding is that a vast majority of the sample (20 objects) is characterized by $kT_e < 100$ keV, and only for two objects we found $kT_e > 200$ keV. The median kT_e for entire sample is 48^{+57}_{-14} keV. The distribution of the y parameter is bimodal, with a broad component centered at ≈ 0.8 and a narrow peak at ≈ 1.1 . A complex, dual absorber model improved the fit for all data sets, compared to a simple absorption model, reducing the fitted strength of Compton reflection by a factor of about 2. Modest reflection (median $R \approx 0.32$) together with a high ratio of Comptonized to seed photon fluxes point towards a geometry with a compact hard X-ray emitting region well separated from the accretion disc. Our results imply that the template Seyferts spectra used in AGN population synthesis models should be revised.

Key words: galaxies: active – galaxies: Seyfert – galaxies: nuclei – X-rays: galaxies – gamma-rays: galaxies.

1 INTRODUCTION

The spectra of Seyfert galaxies in the hard X-ray and soft γ -ray band can be well approximated by a power-law model with a high-energy cut-off accompanied by a Compton reflec-

tion component (for a review see e.g., Beckmann & Shrader 2012). Evidence for that was collected already by the *CGRO* (e.g., Zdziarski et al. 2000) and *BeppoSAX* satellites (e.g., Dadina 2007). Since the late 1990s there is a consensus that the main mechanism responsible for this emission is the thermal Comptonization of seed photons in the plasma cloud surrounding a black hole (BH) in the centre of the AGN (e.g., Svensson 1999). Unfortunately, due to a limited sensitivity of the instruments a detailed quantitative analysis using a physical Comptonization model instead of a phenomenological one is not common. The most sensitive soft γ -ray detector so far, OSSE onboard *CGRO*, excluded the presence of a strong non-thermal emission in Seyferts

^{*} Based on observations with *INTEGRAL*, an ESA project with instruments and science data centre funded by ESA member states (especially the PI countries: Denmark, France, Germany, Italy, Switzerland, and Spain), the Czech Republic, and Poland and with the participation of Russia and the US.

[†] E-mail: P.Lubinski@if.uz.zgora.pl

[‡] present address: Observatoire Français des Tornadoes et des Orages Violents

(Zdziarski et al. 1995). There remains, however, a rather large uncertainty about the typical temperature kT_e of the electrons forming the plasma cloud and the mean Thomson optical depth τ of this region. The studies based on the data from OSSE and other contemporary satellites point towards a low mean temperature $kT_e \simeq 70\text{--}80$ keV and a large optical depth $\tau \simeq 1.7$ (Zdziarski, Poutanen & Johnson 2000). On the other hand, Petrucci et al. (2001) found high values of $kT_e \simeq 170\text{--}320$ keV and small $\tau \simeq 0.05\text{--}0.20$ for 6 Seyfert type 1 galaxies observed by *BeppoSAX*.

The *INTEGRAL* (Winkler et al. 2003) and *Swift* (Gehrels et al. 2004) satellites, despite the detectors not being as sensitive above 50 keV as OSSE, improved the situation thanks to their large field of view resulting in a long total exposure time and a better spatial resolution than OSSE and *BeppoSAX*/PDS, important for more crowded fields. Two other contemporary hard X-ray satellites, *Suzaku* (Mitsuda et al. 2007) and *NuSTAR* (Harrison et al. 2013), are suited more for the shorter observations of single objects, due to their smaller field of view. *NuSTAR* hosts the most sensitive detectors in the 10–80 keV band and provides high-quality spectra but cannot help with constraining a cut-off energy well above 100 keV. Therefore, a comprehensive analysis of average hard X-ray spectra for a larger sample of AGN can be performed predominantly with the *INTEGRAL* and *Swift* data.

Reliable estimates of the plasma temperature and optical depth are crucial elements for drawing a picture of the central engine of AGN. Another such element is the knowledge of the system geometry, in particular the extent of the plasma region and its location relative to the accretion disc. As it was demonstrated for NGC 4151, even in the case of the bright state of this brightest Seyfert galaxy the quality of the spectra does not allow to distinguish which geometry option of the Comptonization model provides the best spectral fit (Lubiński et al. 2010). Thus, until much better spectra are provided by future satellites for the plasma geometry studies (Petrucci 2008), additional information is needed to constrain the structure of the system. The most promising is the Compton reflection component, originating in the accretion disc and torus illuminated by the central X-ray source.

Compton reflection was found to be a common feature of Seyfert spectra already by the *GINGA* satellite (Nandra & Pounds 1994). Further analysis of the AGN and Galactic BH data revealed that the strength of the Compton reflection R relative to a reflection from an infinite slab is quite strongly correlated with the photon index Γ of the X-ray spectra (Zdziarski et al. 1999). This correlation together with the X-ray flux/ Γ correlation support a scenario with a feedback between a hot Comptonizing cloud and a cold reflecting medium in the vicinity of the central black hole (Zdziarski et al. 2003). One of the possibilities explaining the observed phenomena is the existence of a hot inner flow surrounded by a colder accretion disc, consistent with an ADAF geometry (e.g., Abramowicz et al. 1995, Yuan 2001). Due to the presence of a second reflector, namely a distant torus or clumpy absorber, the situation for AGN is more complex than for binary systems and an interpretation of the Γ - R correlation is not straightforward. However, as demonstrated for NGC 4151, good quality data for both low- and high-flux states can be used to disentangle the reflection from the disc and from the torus (Lubiński et al. 2010).

Information about kT_e and τ of the plasma and R of the reflecting medium can be affected by some limitations. First of all, it is quite common that the hard X-ray spectra from *BeppoSAX*, *RXTE*, *INTEGRAL*, *Suzaku* and *Swift* used for the spectral fit lack a clear detection above 100 keV or even below. This makes the analysis of a high-energy cut-off present in both primary Comptonized and reflected components less reliable. Thus, for example, any result placing kT_e well above the upper limit of the spectrum appears dubious. Another limitation comes from the spectral models applied. Phenomenological models typically assume a power-law with an exponential cut-off, which is not as sharp as the cut-off predicted by Comptonization models (Zdziarski et al. 2003). This, in turn, can lead to biased results for the reflected component, when the primary component has an unphysical form.

The cosmic X-ray background (CXB) is expected to be the sum of the emission from the supermassive BH accreting systems (e.g., Mushotzky et al. 2000). Therefore, the CXB spectrum, peaked at around 30 keV, provides a strong constraint on the cut-off energy of a typical AGN. The AGN population synthesis models reproduce the CXB emission assuming that the main constituent of the CXB spectrum below 200 keV is the accumulated emission from Seyfert galaxies. Template spectra used in these models are in the form of the absorbed power-law model with the photon index Γ in the 1.8–1.9 range and the exponential cut-off energy E_C in the 150–400 keV range (e.g., Gilli et al. 2007; Ueda et al. 2014), accompanied by a Compton reflection with R typically around 1. The Comptonization spectra can be approximated by the power-law cut-off model with $E_C = 2\text{--}3 kT_e$, thus the plasma temperature in Seyferts should not usually exceed 200 keV. Nevertheless, due to a lack of detection of the emission above 200 keV for a large Seyfert sample the actual E_C remains quite uncertain and affects the predictions of the synthesis models (Gilli et al. 2007).

The main goal of this work is a comprehensive spectral analysis of the high-quality medium/hard X-ray and soft γ -ray spectra of a large sample of Seyfert galaxies using a realistic, physical model. For this we use the hard X-ray/soft γ -ray data collected by the IBIS/ISGRI detector (Lebrun et al. 2003) onboard the *INTEGRAL* satellite over many years for 28 Seyferts. These summed ISGRI spectra are accompanied by all contemporary medium X-ray (3–18 keV) spectra from the *XMM-Newton*, *Suzaku* and *RXTE* satellites, in order to model the spectral slope and absorption that cannot be studied with the ISGRI spectrum alone. The high-quality data from *XMM-Newton*/EPIC pn and *Suzaku*/XIS allow a much better determination of the spectral parameters than it was possible with the X-ray detectors used with the OSSE data and those onboard of *BeppoSAX*. Compared to the analysis of *BeppoSAX*, *Suzaku* and *NuSTAR* data from relatively short duration observations, our analysis should provide a better description of the mean spectral properties.

2 DATA SELECTION AND REDUCTION

Our sample was selected from the second *INTEGRAL* AGN catalog (Beckmann et al. 2009). We chose all the sources with a total ISGRI effective exposure time larger than

500 ks¹. There are two more sources, namely NGC 4945 and Circinus galaxy, which fulfil the exposure criterion but we excluded them from our sample because their spectra are dominated by the reprocessed component.

Table 1 summarizes the basic physical properties of our sample. There are 8 type 1, 8 intermediate and 12 type 2 Seyfert nuclei, with at least one radio-loud object in each group. The BH mass estimates listed in Table 1 are the weighted mean of all estimates we found in the literature, as well as our estimates based on stellar velocity dispersion measurements, σ_* . The data we used for the BH mass estimation, together with a brief description of the averaging procedure, are presented in Appendix A. The sources in our sample span a BH mass range of almost 3 orders of magnitude.

A summary of the observations we used for the spectral analysis is given in Table 1. Table B1 in Appendix B presents details of the selected spectral sets. We considered all the data collected by *INTEGRAL* as of end of March 2010, except for 4U 0517+17, NGC 4151, MCG+8-11-11, NGC 4388, NGC 2110, NGC 5252 and ESO 103-35, because a large fraction of their data became public after that time (see Table B1). Since the *INTEGRAL* data were collected over many years, the summed ISGRI spectrum corresponds to the averaged emission of the objects in our sample.

We selected data with off-axis angle $< 15^\circ$ ² and we reduced them using the Offline Scientific Analysis (OSA) v. 9.0 provided by the INTEGRAL Science Data Centre (Courvoisier et al. 2003). The standard spectral extraction software was used to extract the ISGRI spectrum for each *INTEGRAL* pointing with the pipeline parameters set to the default values. We created an input source catalog including all sources detected within 15° from each studied object. The ISGRI spectra were summed and the ancillary response files (ARFs) corresponding to them were generated using the OSA tool `spe_pick`.

In the medium X-ray band we supplemented the ISGRI data with data from all available observations of the objects in our sample taken by *XMM-Newton*, *Suzaku* and *RXTE*. The *XMM-Newton*/EPIC pn spectra were extracted using SAS 9.0.0 and the calibration files (CCF) as of 2009 October 21. The *RXTE*/PCA and *Suzaku*/XIS spectra were extracted using HEASOFT 6.8.0 and the calibration files released before March 2010 through CALDB. For several objects we added to the spectral sets the *XMM-Newton* and *Suzaku* spectra collected in years 2010–2013. These new spectra were extracted with SAS 13.5.0 and CCF of 2014 April 11 (*XMM-Newton*) and HEASOFT 6.16 and CALDB released on 2011 June 30 (*Suzaku*). In the case of the *Suzaku*/XIS we reprocessed the 3×3 and 5×5 mode events and we merged them before the spectral extraction. The spectra of the front-illuminated CCDs (XIS0, XIS2 and XIS3) were added together, whereas the spectrum of the back-illuminated detector, XIS1, was used separately. We applied the standard method for extracting the XIS source spectra with the radius of the extraction region set to 250

pixels. However, for the background spectra we used several (two or three) smaller regions with a 125 pixels radius, as close to the source as possible. In this way we avoided the presence of instrumental background lines seen in the background spectra when extracted for larger regions. Depending which *RXTE*/PCA PCU units were switched on during a given observation, we prepared the summed PCU 0+2 or PCU 2 spectra, merging all the data of a given observation ID.

3 SPECTRAL ANALYSIS

3.1 Model definition

Spectral fitting was performed with XSPEC v. 12.7.0 (Arnaud 1996). Errors are given for 90 per cent confidence level for a single parameter, $\Delta\chi^2 = 2.7$.

For ISGRI we used the 18–200 keV range, except for 4U 0517+17, ESO 103-35 and LEDA 170194 where the spectra above 112 keV were affected by strong background fluctuations, as the observations of these sources were made predominantly at large off-axis angle. To limit the complexity of the fitted models, we did not consider X-ray data at energies below 3 keV. An additional rationale to not use the data below 3 keV is that, when we included them, the low-energy data dominated the fit in most sources. As a result, the ISGRI model fit worsened; large residuals appear above 20 keV and both the high-energy cut-off energy and the reflection fraction are not well determined. Consequently, the EPIC pn, the XIS0-3 and the XIS1 spectra were used in the 3–10 keV, 3–10 keV and 3–9 keV bands, respectively. The only exceptions were ESO 141-55, Mrk 509, 4U 0517+17 and LEDA 170194, for which we included the 1–3 keV data to the fit. The first two sources show a strong soft excess extending above 3 keV, where the data were insufficient to constrain the absorption and excess parameters at the same time. The two other sources were among the weakest sources in our sample, in addition with only two low-energy observations for each. Thus, the extended low-energy spectra were needed to obtain a reasonable fit. The PCA PCU spectra were fitted in the 5–18 keV band. We excluded channels below 5 keV because we found that the standard correction of the xenon L-edge absorption at ~ 4.1 keV is not sufficient for the weak sources in the sample, and the residuals in this band were affecting the overall χ^2 value.

The model we adopted for spectral fitting is the following (in XSPEC terminology): `CONSTANT*WABS*ZWABS*ZXIPCF*(COMPPS+ZGAUSS[+ZGAUSS])`. This is identical to the model used by Lubiński et al. (2010) in the case of NGC 4151, except that we have replaced the partial absorber model `ZPCFABS` by `ZXIPCF` which accounts for an ionized absorber partially covering the central source.

The component which accounts for the primary X-ray continuum emission is `COMPPS`. This is a model for the estimation of thermal Comptonization spectra computed for different geometries using the exact numerical solution of the radiative transfer equation (Poutanen & Svensson 1996). The model also includes Compton reflection of the Comptonized emission from the cool medium (Magdziarz & Zdziarski 1995). We fitted the spectra allowing for four free parameters for this component: the tem-

¹ Corresponding to an observation with the source in the fully coded field of view.

² $< 6^\circ$ for 4U 0517+17 due to its proximity to the Crab, which is contaminating the ISGRI shadowgrams.

Table 1. Sample of studied Seyfert galaxies and summed exposure time for each satellite. The objects in each group (Sy 1, Sy 1.5, Sy 2) are sorted in order of decreasing 20–100 keV flux. Central black hole masses M_{BH} are computed as a weighted mean of the values from the literature (see the text and Appendix A). The number of extracted spectra for each low-energy satellite is given in parentheses.

Object	Redshift	$\log(M_{\text{BH}})$ [M_{\odot}]	<i>INTEGRAL</i>	<i>XMM-Newton</i>	<i>Suzaku</i>	<i>RXTE</i>
Exposure time [ks]						
Type 1						
IC 4329A	0.0160	8.02 ± 0.17	1774	150 (2)	131 (5)	382 (6)
IGR J21247+5058	0.0200	7.80 ± 0.50	5656	40 (2)	85 (1)	—
GRS 1734-292	0.0214	8.94 ± 0.30	15214	18 (1)	—	—
NGC 4593	0.0090	7.13 ± 0.08	2962	81 (2)	119 (1)	902 (6)
4U 0517+17	0.0179	7.18 ± 0.14	2399	62 (1)	46 (1)	—
Akn 120	0.0337	8.18 ± 0.06	2209	112 (1)	101 (1)	114 (1)
ESO 141-55	0.0366	7.60 ± 0.24	979	213 (4)	—	—
3C 111	0.0485	8.04 ± 0.19	2676	169 (2)	122 (1)	676 (5)
Type 1.5						
NGC 4151	0.0033	7.43 ± 0.11	3236	354 (11)	247 (3)	—
MCG+8-11-11	0.0205	8.02 ± 0.04	1404	38 (1)	99 (1)	17 (1)
Mrk 509	0.0344	8.18 ± 0.04	1371	704 (6)	108 (4)	439 (3)
4U 1344-60	0.0130	7.67 ± 0.36	5781	37 (1)	94 (1)	—
3C 120	0.0331	7.79 ± 0.10	1721	146 (2)	165 (4)	1049 (5)
NGC 6814	0.0052	7.14 ± 0.11	3664	32 (1)	42 (1)	19 (1)
3C 390.3	0.0562	8.53 ± 0.08	1794	123 (2)	100 (1)	247 (2)
MCG-6-30-15	0.0079	6.86 ± 0.18	2174	462 (5)	384 (4)	468 (5)
Type 2						
NGC 4388	0.0084	7.05 ± 0.09	4815	73 (2)	124 (1)	—
NGC 2110	0.0076	8.21 ± 0.18	1736	60 (1)	102 (1)	180 (2)
NGC 4507	0.0118	7.71 ± 0.18	1600	117 (5)	104 (1)	137 (2)
MCG-5-23-16	0.0085	7.45 ± 0.20	839	157 (2)	96 (1)	159 (2)
NGC 5506	0.0062	7.31 ± 0.18	1479	264 (6)	159 (3)	167 (2)
Cygnus A	0.0561	9.41 ± 0.10	5614	41 (2)	45 (1)	—
NGC 5252	0.0222	8.47 ± 0.18	3674	67 (1)	50 (1)	—
ESO 103-35	0.0132	7.21 ± 0.22	1090	13 (1)	91 (1)	132 (1)
NGC 788	0.0136	7.45 ± 0.19	2136	35 (1)	46 (1)	—
NGC 6300	0.0037	6.63 ± 0.22	3580	53 (1)	83 (1)	26 (1)
NGC 1142	0.0288	8.40 ± 0.21	1629	12 (1)	142 (2)	—
LEDA 170194	0.0367	8.58 ± 0.50	1135	17 (1)	130 (1)	—

perature kT_e of the plasma cloud, the Compton parameter y , the reflection parameter R , and the normalization of the seed photons spectrum K . The Compton parameter can be used to determine the Thomson optical depth τ of the plasma cloud using the relation $\tau = ym_e c^2 / (4kT_e)$, where m_e is the electron mass (e.g., Rybicki & Lightman 1979). The seed photons were assumed to have a multicolor disc blackbody distribution (DISKBB in XSPEC, Mitsuda et al. 1984) with the maximum temperature of $kT_{\text{bb}} = 10$ eV. As we have tested, fixing the maximum disc temperature at other value, e.g., 100 eV, does not affect the fit results considerably.

The COMPPS model offers several options for geometry of the plasma region but, as shown for NGC 4151 (Lubiński et al. 2010), none of them is statistically preferred even for the fit done to the highest-quality AGN spectra. Thus, we decided to use the simplest geometry option: a spherical case with an approximate treatment of radiative transfer using escape probability (denoted in COMPPS by the geometry parameter = 0). The inclination angle of the reflector was set to $i = 30^\circ$, 45° and 60° for type 1, 1.5 and 2 Seyferts, respectively. The reflector was assumed to be neutral, and relativistic broadening of the reflected spectra was ignored. Although the relativistic reflection from an ionized disc can be fitted to the spectra of particular AGN (e.g.,

Reynolds 2014), these effects will be weak above 3 keV. We have tested this assumption for MCG-6-30-15, an archetypical AGN with relativistic effects, finding the relaxed disc ionization consistent with 0.

We added a redshifted Gaussian line to the primary emission component to model the iron K α emission from the host galaxy. For many objects we had also to include a second Gaussian corresponding to the iron K β emission. The iron line parameters were fitted independently for each low-energy spectrum.

In addition to the continuum emission we also considered the case of absorption of the primary emission. The absorption consisted of three sub-components: Galactic (component WABS) and redshifted neutral absorbers (ZWABS), and redshifted ionized, partially covering absorber (ZXIPCF). The WABS and ZWABS models use the elemental abundances of Anders & Ebihara (1982) and the photoelectric absorption cross-sections from Morrison & McCammon (1983). The Galactic column density was set to a weighted mean given by the nH HEASARC tool and computed using the data from Kalberla et al. (2005).

The model ZXIPCF uses a grid of XSTAR photoionized absorption models (calculated assuming a microturbulent velocity of 200 km s^{-1}) for the absorption. It assumes that

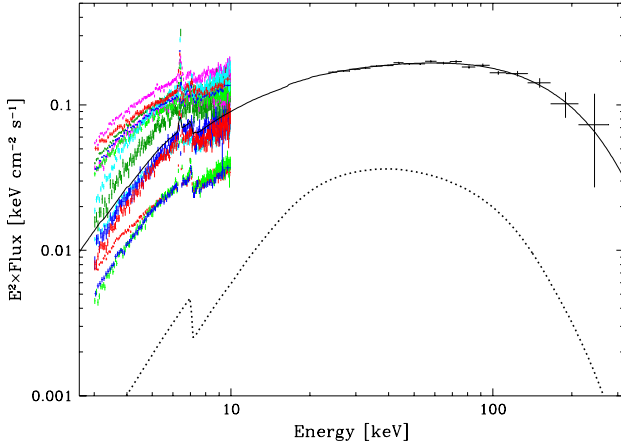


Figure 1. Spectral modelling (option D) applied to the spectra of NGC 4151. The unfolded ISGRI spectrum is shown in black and spectra taken with *XMM-Newton* and *Suzaku* are shown in colour. The solid line shows an absorbed continuum model (with reflection) fitted to the ISGRI spectrum, the dotted line shows the reflection component. The models fitted to the low-energy spectra are not shown.

the absorber covers some fraction f^p of the source, while the remaining fraction $(1 - f^p)$ of the spectrum is seen directly (Reeves et al. 2008). Apart from f^p , the other parameters of this component are the column density of the ionized absorber N_H^p and the logarithm of the ionization parameter ξ^p . The ionization parameter ξ^p for *RXTE*/PCA, the instrument with a low energy resolution, was set to the mean value obtained for the *XMM-Newton*/EPIC pn and *Suzaku*/XIS spectra. After test fits we found that two other parameters of the complex absorber model, namely N_H^p and f^p , have to be fixed to the mean obtained for the *XMM-Newton* and *Suzaku* spectra, because the limited energy range of the *RXTE* spectra does not allow to constrain these parameters well.

For the pairs of *Suzaku*/XIS front and back-illuminated spectra we assumed the same spectral slope and absorption but their relative normalizations and parameters of iron lines were allowed to be different, to account for the difference in their absolute calibration and energy resolution. After some initial tests we applied a 3 per cent systematic error to the *Suzaku*/XIS spectra, all other spectra were fitted with the statistical errors only.

For two sources with the *XMM-Newton* and *Suzaku* spectra fitted in the 1–10 keV band, namely ESO 141-55 and Mrk 509, we had to add several additional components. In the case of ESO 141-55 these were two absorption edges around 2.1 and 2.6 keV (XSPEC model ZEDGE), bremsstrahlung emission model (ZBREMS) for the soft excess and an additional emission line at ≈ 2.5 keV. Only one absorption edge at ≈ 1.8 keV was needed for the Mrk 509 spectra, together with the bremsstrahlung component modelling the soft excess.

3.2 Model options

For each source the ISGRI spectrum and all low-energy X-ray spectra were fitted simultaneously with the model described above. The ISGRI spectra are collected over a long

Table 2. Summary of the spectral model options applied in the fit. The parameters allowed to be different for each low-energy spectrum are checkmarked, whereas the parameters not present in the model Ba are marked with em-dash.

Model option	Parameter					
	n_I	y	N_H	N_{H^p}	f_p	$\log \xi_p$
A	✓					
B	✓	✓				
Ba	✓	✓		—	—	—
C	✓		✓	✓	✓	✓
D	✓	✓	✓	✓	✓	✓

time, while the low-energy observations are usually short, especially in the case of *XMM-Newton* and *Suzaku*. These observations should provide information about “short” term spectral variations for each object. Regarding these variations, we considered the possibility of spectral slope and/or warm absorber variations. We did not consider variations of kT_e and R , as these parameters cannot be determined from the model fits to the individual low-energy spectrum separately, due to their limited energy coverage. For that reason, during the spectral fits we kept kT_e and R tied to the same value for all spectra.

Table 2 summarizes the different variability options that we considered for the spectral slope and absorption. First we fitted all the data sets for each object assuming no spectral variations, i.e., all the model parameters were kept tied to the same value, for all spectra, apart from the model normalization which was always allowed to vary (model A). Then we assumed that only the spectral slope, characterized by y , was variable (model B) or that only the absorption was variable (model C). We also considered the possibility that both the spectral slope and the absorption was variable (model D). In addition to the model options presented already, for each object we made a fit alternative to model B, denoted as Ba, with the partially covering absorption component removed. This test allowed us to judge how the choice of the absorption model, done in various analyses, affects the results.

During all model fits the ISGRI normalization was fixed at 1. Depending on the model version we were fitting to the data, the model parameters ‘checked’ in Table 2 were left as free variables for all low-energy spectra. The respective model parameter for the ISGRI spectrum was kept fixed to the arithmetic mean of all the best-fitting parameter values determined from each one of the low-energy spectra. The other continuum model parameters were kept tied to the same value during the fit, for all spectra. In summary, our approach assumes that the ISGRI spectrum represents the average spectral shape for all objects in our sample, while the low-energy spectra can be used to detect temporal deviations of the spectral slope (models B, Ba, D) and warm absorption (models C, D) from the respective average model parameter values.

An illustration of our spectral modelling is presented in Figure 1, showing an entire spectral set used for the NGC 4151 study together with the total and reflection models fitted to the average spectrum. The data from *XMM-Newton* and *Suzaku* show a range of variability observed for the low-energy spectra. Figure 2 presents the examples of

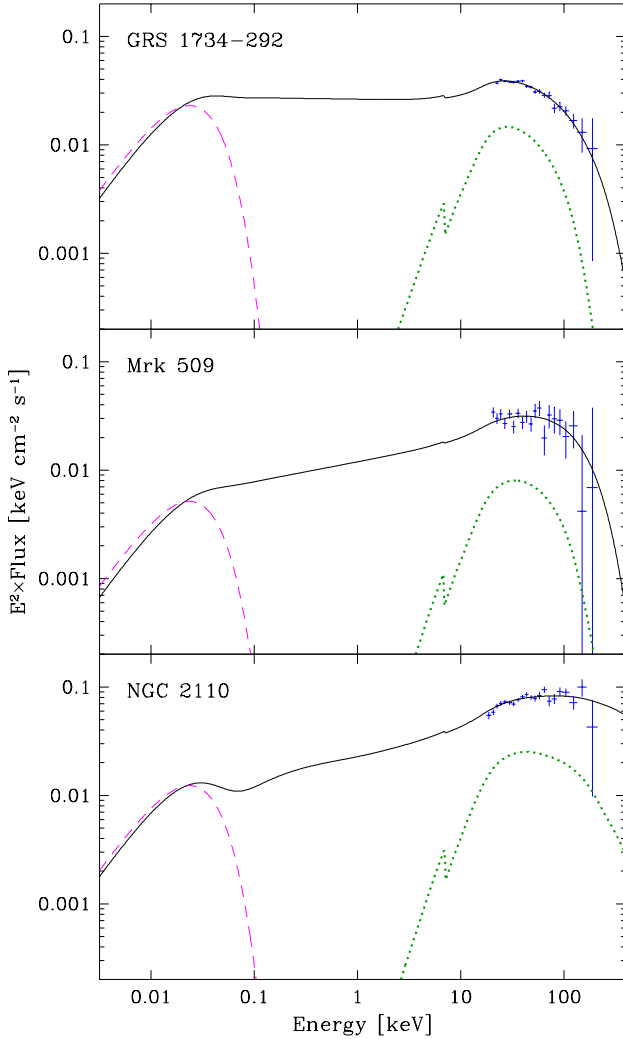


Figure 2. Unfolded ISGRI (blue) spectra of GRS 1734-292, Mrk 509 and NGC 2110. Solid line - an unabsorbed Comptonization plus reflection model, dashed line - multi-colour black body model of seed photons, dotted line - the reflection component.

the best model fitted to the spectral sets of GRS 1734-292, Mrk 509 and NGC 2110. In this figure we show only the mean model corresponding to the ISGRI spectrum and the ISGRI data. Note the high quality of the GRS 1734-292 spectrum, thanks to the 15 Ms exposure time. This spectrum also shows that the ISGRI spectra extracted with OSA 9 are not affected by strong systematic features: data points agree with the model within the error bars. The rest of the ISGRI spectra is presented in the Appendix C.

During the spectral fitting our major concern was a careful test if the global χ^2 minimum was found for a given model option and data set. Modelling with XSPEC or any other spectral software cannot be fully automatized, especially when the model is complex and the spectra have a large number of channels. Therefore we performed initial tests looking for the best-fitting value of K , kT_e , y and R parameters, scanning their values in a wide range using the XSPEC `steppar` command. Then we computed in the same way the uncertainties for all other free parameters. Finally, the fit was checked running two-dimensional scan for several

pairs of parameters: $kT_e - R$ for model options B and D and $kT_e - R$, $kT_e - y$ and $y - R$ for model option C. Whenever we found a new χ^2 minimum during one of these phases of analysis, all the phases were repeated until there was no more fit improvement.

3.3 Method limitations

The most correct way of determining the average spectral properties of any class of objects is to compute a weighted mean for the parameters determined for possibly short observations sampling frequently a possibly long period. However, the number of emitted photons and instrumental background change rapidly with increasing energy in the X-ray and soft Γ -ray domain, reducing strongly data quality in the high-energy band. For this reason the parameters driven mainly by that band cannot be well determined with the short exposure time spectra. Our strategy of using the summed ISGRI spectra allows us to find accurate mean values of kT_e and R at the cost of a model where some parameters are set to the mean and some are fitted separately to the low-energy spectra. Thus, the determined values of kT_e and especially R can be biased in situation when both these quantities vary between low-energy observations. A scale of that bias can be estimated with the fit done to the spectra simulated with the models assuming various plausible variability patterns. Since finding a global χ^2 minimum for a single case is work intensive and time consuming as described above, a massive fitting of simulated spectra is practically impossible. Instead, we have tried several simpler ways to check the reliability of our results.

One of these tests is the application of various model options presented above. For a vast majority of studied Seyferts the results of models B, C and D assuming variable Compton parameter and/or absorption appeared quite similar (see Table 4). On the other hand, we included in our sample the X-ray brightest Seyfert, namely NGC 4151, for which an analysis of the flux-resolved spectral sets, including contemporary low- and high-energy spectra, was done earlier with a similar complex model (Lubiński et al. 2010). The mean kT_e , y and R values found here (see Table 3) are very similar to those determined by Lubiński et al. (2010) for the bright state of NGC 4151. This is expected as the summed spectrum will be always dominated by the bright state, which in addition prevails in the *INTEGRAL* observations. Thus, at least for NGC 4151 our ‘average’ approach produces reasonable results. In addition, for this bright object we did a special fit with R fitted separately for each low-energy spectrum. Although the fitted R values vary between 0 and 1.4, their mean equal to $0.34^{+0.12}_{-0.07}$ is almost the same as that fitted with model D. The kT_e and y values do not change as well. Therefore, a constant R approximation appears to be justified.

4 RESULTS

4.1 The best-fitting model selection

The best-fitting results for all model options should be compared in a quantitative way to choose the final result for a given object. A commonly applied criterion to convert the

χ^2 values obtained for two models into their relative probability measure is the F -test. Although this test is justified in many situations, its assumptions allowing for a computing of the probability P_F based on the F -distribution are not always met. When the models are not nested or when the interesting parameter is set to its boundary limit in the simpler model, the true distribution can be far from the reference test distribution (Protassov et al. 2002). The model options used in our analysis violate both these conditions. Despite the fact that we use the same general XSPEC model form for all alternatives, any operation tying one parameter to the other, e.g., when the absorption or Compton y parameters are computed as an average for the ISGRI spectrum, breaks the nesting condition. The second assumption is not met when we fix, for example, the N_H^P and f^P parameters of the complex absorber component to zero, fitting the simple absorption model option Ba.

Model selection is still an open issue of the contemporary statistics, with various selection methods showing their pros and cons (e.g., Wit et al. 2012). One of the most general and robust tests is the Bayesian model comparison, either in the form of exact Bayes factors or reduced to the Bayesian information criterion (BIC). Since the Bayesian analysis is computationally demanding, we decided to use an easy to compute and robust test in the form of the Akaike information criterion (AIC, Akaike 1973), for which the nesting condition is not required. To take into account a bias introduced by a finite size of the sample, we applied a corrected AIC test (Sugiura 1978), which for the χ^2 -statistic used for a spectral fit has the form

$$AIC_C = 2k - 2C_L + \chi^2 + \frac{2k(k+1)}{n-k-1}, \quad (1)$$

where C_L is the likelihood of the true hypothetical model and does not depend on the data or tested models, k is the number of free parameters of a given model and n is the total number of the channels in the fitted spectra. Since the models are compared through computing a difference of their AIC_C values, the constant C_L cancels out. The relative likelihood p_A that the more complex model b is better than its simpler alternative s is given by the exponential $p_A = \exp[0.5(AIC_C^s - AIC_C^b)]$. In our case, the reference (most complex) model was the model D, to which all other simpler model options were compared.

The Akaike criterion strongly favours the models with fewer parameters due to the terms with the free parameter number k . In the case of our analysis models B with a variable spectral slope are favoured over the models C with a variable absorption, because the latter need three free parameters more for a single low-energy spectrum. The X-ray absorption varying on time scales of days, months or years is a well established fact for the Seyfert galaxies, whenever a high-quality spectral sets were available (e.g., Puccetti et al. 2007; Turner & Miller 2009). Thus, the penalty of more complex models introduced with the Akaike test appears too strong. We observe typically much larger uncertainties of the kT_e , y and R values for model B than for models C and D. This indicates that the variability of the y parameter is not sufficient to explain the observed spectral variability. For this reason we decided to add an additional model selection criterion, requiring the lowest χ^2 for the ISGRI spectrum alone. This addition is strongly required as the two basic pa-

rameters we seek, namely kT_e and R , are determined mainly by the ISGRI spectrum. Consequently, the final model selection criterion was: a model with the highest p_A value that is giving the lowest χ^2 for the ISGRI spectrum.

4.2 The best-fitting results

Table 3 presents the summary of the spectral fitting results, showing only the parameters of the best mean continuum model selected for each object. The most complex model option D, assuming variable both spectral slope and absorption, almost always resulted in the smallest best-fitting χ^2 value. The only exception was GRS 1734-292 with a single low-energy spectrum, thus allowing to fit only model option A. Only half of the D option cases passed the Akaike criterion test preferring a simpler option A, B or C. A secondary criterion selecting the model option with the smallest χ^2 value for the ISGRI spectrum had to be applied only three times, changing the choice from model C to D for 4U 0517+17 ($\Delta\chi^2/\chi^2 = 0.3/16.0$) and from model B to D for MCG+8-11-11 ($\Delta\chi^2/\chi^2 = 1.0/36.0$) and for 3C 120 ($\Delta\chi^2/\chi^2 = 1.5/20.9$). Model B with the varying low-energy spectral slope appeared the best for 5 objects, mainly those less absorbed. For 7 objects the best choice was option C with variable absorption. The number of high-quality low-energy spectra strongly determines the best model form: for all cases where there were at least 4 spectra taken with either *XMM-Newton* and/or *Suzaku* the best model is model D. We conclude that, apart from significant flux variations, Seyferts usually show significant spectral slope and/or warm absorbing variations as well.

Besides the parameters fitted directly to the spectra with a model defined in Sec. 3.1 we have computed three other parameters based on the fit results. The first is the photon index Γ used commonly in phenomenological power-law models approximating the continuum of the X-ray spectra of accreting systems. To compute a value of Γ corresponding to our results, we simulated a large number of *XMM-Newton* spectra with the COMPPS model and a dense grid of (kT_e, y) values. These spectra were fitted in the 2–10 keV band with a power-law model, providing an array of Γ values. Then the Γ value for each (kT_e, y) pair, determined with the COMPPS model for our AGN sample, was computed with a two-dimensional interpolation. The Thomson optical depth τ of the plasma was computed using the best-fitting values of the kT_e and y parameters (see Sec. 3.1). Since the number of Compton scatterings considered in the COMPPS model is limited, the τ value computed this way can be incorrect. The authors of the code warn of situations where $\tau > 3$ and this limit is exceeded for many spectral sets fitted here. Therefore all τ values were checked with a Monte Carlo code simulating the Comptonization process (Gierliński 2000), based on a model of Górecki & Wilczewski (1984). The fitted kT_e was assumed and then the simulated τ_{MC} was adjusted to obtain the same spectral shape above 1 keV as that given by COMPPS model. The optical depth derived from simulations is usually smaller than the one derived from the COMPPS model by about 30–40 per cent.

Figure 3 presents the distributions of values of the three main parameters of the continuum model and Γ values found for the whole sample with selected best-fitting model. The distributions of kT_e , R and Γ values are asymmetric and do

Table 3. Main results of the spectral fitting. Comptonization model parameters: kT_e - electron plasma temperature in keV; y - Compton parameter; τ - plasma optical depth; R - relative amplitude of the reflection component; K - absolute normalization of the seed photons spectrum in 10^8 . Other COMPPS parameters were fixed: the temperature of the seed photons (a multi-colour black body) $T_{bb} = 10$ eV, the inclination angle $i = 30^\circ$ (Sy 1), 45° (Sy 1.5), 60° (Sy 2), the disc temperature $temp = 10^5$ K. Other parameters: N_H , N_H^P - column density of neutral and ionized, partially covering absorbers, respectively, in 10^{22} cm^{-2} , f^P and ξ^P (in erg cm s^{-1}) - covering fraction and ionization parameter, respectively, of partial, ionized absorber. The photon index Γ and the plasma optical depth τ_{MC} were computed in a way described in the text. For model options see Table 2.

Object (model)	kT_e	R	K	y	Γ	τ	τ_{MC}	N_H	N_H^P	f^P	$\log \xi^P$	χ^2_{red}
IC 4329A (D)	40^{+7}_{-5}	$0.12^{+0.04}_{-0.04}$	$3.75^{+0.56}_{-0.14}$	$0.95^{+0.02}_{-0.02}$	$1.87^{+0.02}_{-0.02}$	$3.0^{+0.4}_{-0.6}$	2.25	$0.43^{+0.17}_{-0.17}$	103^{+14}_{-10}	$0.23^{+0.04}_{-0.02}$	$1.62^{+0.15}_{-0.19}$	0.90
IGR J21247+5058 (C)	35^{+10}_{-6}	$0.11^{+0.25}_{-0.11}$	$0.93^{+0.27}_{-0.17}$	$1.14^{+0.05}_{-0.06}$	$1.74^{+0.04}_{-0.03}$	$4.2^{+0.8}_{-1.2}$	2.9	$2.4^{+0.4}_{-0.8}$	102^{+50}_{-27}	$0.35^{+0.16}_{-0.09}$	$0.7^{+0.6}_{-1.3}$	0.95
GRS 1734-292 (A)	49^{+20}_{-16}	$0.66^{+0.39}_{-0.44}$	$3.42^{+2.23}_{-0.96}$	$0.78^{+0.07}_{-0.07}$	$2.01^{+0.12}_{-0.07}$	$2.0^{+0.7}_{-0.9}$	1.73	$2.8^{+0.4}_{-1.4}$	31^{+391}_{-21}	$0.27^{+0.13}_{-0.09}$	$-0.6^{+1.1}_{-2.4}$	1.08
NGC 4593 (B)	27^{+6}_{-4}	$0.0^{+0.07}_{-0.0}$	$0.61^{+0.13}_{-0.07}$	$1.09^{+0.02}_{-0.02}$	$1.77^{+0.01}_{-0.02}$	$5.2^{+0.8}_{-1.1}$	3.45	$0.0^{+0.24}_{-0.0}$	143^{+28}_{-21}	$0.22^{+0.02}_{-0.03}$	$2.84^{+0.07}_{-0.07}$	1.00
4U 0517+17 (D)	32^{+16}_{-8}	$0.40^{+0.30}_{-0.35}$	$0.42^{+0.08}_{-0.07}$	$1.09^{+0.05}_{-0.05}$	$1.77^{+0.03}_{-0.03}$	$4.35^{+1.11}_{-2.19}$	3.0	$0.06^{+0.01}_{-0.02}$	$8.8^{+2.5}_{-4.0}$	$0.61^{+0.05}_{-0.25}$	$1.46^{+0.46}_{-0.48}$	0.90
Akn 120 (D)	179^{+23}_{-28}	$0.49^{+0.16}_{-0.19}$	$8.39^{+1.13}_{-1.53}$	$0.44^{+0.04}_{-0.03}$	$2.13^{+0.02}_{-0.07}$	$0.31^{+0.06}_{-0.05}$	0.24	$0.05^{+0.40}_{-0.05}$	44^{+10}_{-7}	$0.30^{+0.04}_{-0.04}$	$-0.86^{+0.92}_{-0.30}$	0.96
ESO 141-55 (B)	138^{+18}_{-33}	$0.77^{+0.14}_{-0.07}$	$2.17^{+0.20}_{-0.17}$	$0.64^{+0.02}_{-0.04}$	$2.02^{+0.09}_{-0.04}$	$0.59^{+0.13}_{-0.09}$	0.47	$0.0^{+0.012}_{-0.0}$	$0.31^{+0.07}_{-0.05}$	$0.37^{+0.03}_{-0.03}$	$-0.27^{+0.03}_{-0.04}$	1.32
3C 111 (B)	113^{+107}_{-68}	$0.26^{+0.08}_{-0.07}$	$1.18^{+1.88}_{-0.16}$	$0.94^{+0.06}_{-0.08}$	$1.84^{+0.10}_{-0.10}$	$1.1^{+0.7}_{-1.0}$	0.85	$0^{+0.8}_{-0.0}$	$4.7^{+14.0}_{-0.8}$	$0.25^{+0.04}_{-0.12}$	$-3^{+3.6}_{-0.0}$	1.05
NGC 4151 (D)	53^{+7}_{-3}	$0.33^{+0.08}_{-0.05}$	$3.41^{+0.33}_{-0.36}$	$1.11^{+0.04}_{-0.04}$	$1.76^{+0.03}_{-0.02}$	$2.68^{+0.18}_{-0.37}$	2.04	$3.7^{+0.9}_{-0.4}$	$21.3^{+1.6}_{-1.4}$	$0.75^{+0.02}_{-0.05}$	$1.06^{+0.06}_{-0.22}$	1.12
MCG+8-11-11 (D)	44^{+23}_{-12}	$0.0^{+0.12}_{-0.0}$	$4.3^{+2.0}_{-1.5}$	$0.85^{+0.05}_{-0.08}$	$1.95^{+0.09}_{-0.05}$	$2.5^{+0.7}_{-1.3}$	1.85	$1.9^{+2.6}_{-1.2}$	100^{+49}_{-9}	$0.43^{+0.10}_{-0.09}$	$0.8^{+0.3}_{-0.9}$	0.83
Mrk 509 (C)	43^{+27}_{-12}	$0.40^{+0.03}_{-0.04}$	$0.76^{+0.04}_{-0.04}$	$1.03^{+0.02}_{-0.02}$	$1.81^{+0.02}_{-0.02}$	$3.1^{+0.9}_{-2.0}$	2.20	$0.04^{+0.10}_{-0.04}$	$1.48^{+0.11}_{-0.18}$	$0.43^{+0.05}_{-0.07}$	$-2.43^{+0.39}_{-0.25}$	1.06
4U 1344-60 (C)	30^{+19}_{-8}	$0.55^{+0.73}_{-0.55}$	$0.62^{+0.28}_{-0.19}$	$1.05^{+0.10}_{-0.08}$	$1.79^{+0.06}_{-0.06}$	$4.5^{+1.3}_{-2.9}$	3.1	$1.9^{+0.5}_{-0.4}$	182^{+99}_{-57}	$0.53^{+0.11}_{-0.13}$	$2.80^{+0.10}_{-0.21}$	0.94
3C 120 (D)	176^{+24}_{-23}	$0.27^{+0.07}_{-0.06}$	$8.2^{+1.8}_{-1.6}$	$0.50^{+0.03}_{-0.03}$	$2.08^{+0.07}_{-0.06}$	$0.36^{+0.05}_{-0.05}$	0.3	$0.52^{+0.19}_{-0.11}$	$36.7^{+4.2}_{-3.4}$	$0.37^{+0.02}_{-0.02}$	$-1.34^{+0.35}_{-0.08}$	0.96
NGC 6814 (C)	46^{+69}_{-14}	$0.0^{+0.22}_{-0.0}$	$0.42^{+0.48}_{-0.13}$	$1.14^{+0.08}_{-0.16}$	$1.74^{+0.08}_{-0.05}$	$3.2^{+1.0}_{-3.2}$	2.35	$0.1^{+1.0}_{-0.1}$	101^{+49}_{-56}	$0.37^{+0.10}_{-0.13}$	$1.86^{+0.28}_{-0.48}$	1.11
3C 390.3 (B)	37^{+44}_{-11}	$0.0^{+0.15}_{-0.0}$	$0.66^{+0.24}_{-0.21}$	$1.06^{+0.03}_{-0.03}$	$1.79^{+0.02}_{-0.02}$	$3.7^{+1.1}_{-3.7}$	2.55	$0.17^{+0.18}_{-0.17}$	81^{+18}_{-33}	$0.21^{+0.02}_{-0.08}$	$1.90^{+0.13}_{-0.45}$	0.96
MCG-6-30-15 (D)	31^{+9}_{-5}	$1.77^{+0.12}_{-0.14}$	$6.25^{+0.48}_{-0.18}$	$0.60^{+0.01}_{-0.01}$	$2.26^{+0.03}_{-0.03}$	$2.5^{+0.7}_{-0.7}$	1.88	$2.35^{+0.21}_{-0.24}$	151^{+46}_{-35}	$0.43^{+0.08}_{-0.09}$	$4.37^{+0.11}_{-0.11}$	1.02
NGC 4388 (D)	53^{+17}_{-9}	$0.07^{+0.17}_{-0.07}$	$1.83^{+0.40}_{-0.26}$	$1.11^{+0.11}_{-0.11}$	$1.76^{+0.07}_{-0.06}$	$2.7^{+0.6}_{-0.9}$	1.92	$20.9^{+1.4}_{-6.4}$	57^{+48}_{-21}	$0.63^{+0.08}_{-0.06}$	$1.79^{+0.13}_{-0.22}$	1.10
NGC 2110 (D)	230^{+51}_{-57}	$0.63^{+0.09}_{-0.16}$	$1.83^{+0.62}_{-0.33}$	$0.94^{+0.10}_{-0.09}$	$1.75^{+0.09}_{-0.06}$	$0.52^{+0.14}_{-0.13}$	0.39	$1.0^{+1.3}_{-0.4}$	$5.9^{+3.7}_{-3.3}$	$0.54^{+0.17}_{-0.17}$	$-0.47^{+0.51}_{-0.16}$	0.89
NGC 4507 (D)	30^{+5}_{-4}	$0.0^{+0.09}_{-0.0}$	$0.84^{+0.29}_{-0.14}$	$1.19^{+0.11}_{-0.13}$	$1.71^{+0.08}_{-0.06}$	$5.1^{+0.8}_{-1.0}$	3.4	$7.1^{+1.8}_{-1.8}$	$54.6^{+3.5}_{-2.5}$	$0.95^{+0.03}_{-0.03}$	$1.13^{+0.09}_{-0.10}$	1.14
MCG-5-23-16 (D)	97^{+38}_{-38}	$0.69^{+0.28}_{-0.22}$	$8.3^{+3.7}_{-2.9}$	$0.69^{+0.09}_{-0.08}$	$2.04^{+0.15}_{-0.12}$	$0.91^{+0.38}_{-0.37}$	0.75	$1.87^{+0.54}_{-0.58}$	$32.5^{+6.7}_{-5.8}$	$0.38^{+0.04}_{-0.04}$	$0.49^{+0.28}_{-0.51}$	0.98
NGC 5506 (D)	28^{+5}_{-3}	$0.31^{+0.06}_{-0.08}$	$5.27^{+0.53}_{-0.46}$	$0.84^{+0.02}_{-0.02}$	$1.97^{+0.02}_{-0.02}$	$3.8^{+0.4}_{-0.7}$	2.7	$4.0^{+0.3}_{-0.2}$	218^{+26}_{-23}	$0.34^{+0.07}_{-0.05}$	$2.69^{+0.04}_{-0.09}$	0.99
Cygnus A (B)	185^{+10}_{-11}	$0.32^{+0.05}_{-0.06}$	$3.46^{+0.18}_{-0.13}$	$0.69^{+0.02}_{-0.02}$	$1.92^{+0.03}_{-0.02}$	$0.48^{+0.03}_{-0.03}$	0.37	$0.0^{+0.4}_{-0.0}$	$11.1^{+2.4}_{-1.4}$	$0.63^{+0.02}_{-0.04}$	$0.35^{+0.25}_{-0.10}$	1.09
NGC 5252 (A)	84^{+491}_{-36}	$0.0^{+0.63}_{-0.0}$	$0.78^{+2.52}_{-0.36}$	$1.12^{+0.12}_{-0.64}$	$1.75^{+0.67}_{-0.07}$	$1.70^{+0.76}_{-1.70}$	1.4	$0.0^{+6.6}_{-0.0}$	$5.8^{+22.3}_{-2.5}$	$0.98^{+0.02}_{-0.88}$	$0.3^{+1.5}_{-3.3}$	0.92
ESO 103-35 (C)	43^{+46}_{-14}	$0.88^{+0.62}_{-0.30}$	$4.24^{+1.92}_{-1.33}$	$0.74^{+0.12}_{-0.08}$	$2.06^{+0.12}_{-0.11}$	$2.20^{+0.75}_{-2.20}$	1.65	$21.1^{+0.5}_{-0.5}$	190^{+94}_{-38}	$0.40^{+0.17}_{-0.13}$	$2.77^{+0.72}_{-0.31}$	0.89
NGC 788 (D)	54^{+44}_{-22}	$0.08^{+1.20}_{-0.08}$	$0.7^{+1.2}_{-0.5}$	$1.06^{+0.21}_{-0.16}$	$1.79^{+0.12}_{-0.12}$	$2.5^{+1.2}_{-2.1}$	1.95	$13.7^{+9.9}_{-9.7}$	101^{+14}_{-29}	$0.99^{+0.01}_{-0.02}$	$1.44^{+0.13}_{-0.10}$	0.98
NGC 6300 (C)	62^{+245}_{-30}	$2.32^{+0.97}_{-0.82}$	$0.61^{+2.54}_{-0.27}$	$0.91^{+0.11}_{-0.50}$	$1.89^{+0.12}_{-0.20}$	$1.9^{+1.0}_{-1.9}$	1.45	$24.2^{+2.4}_{-2.4}$	178^{+87}_{-124}	$0.69^{+0.15}_{-0.19}$	$4.25^{+0.41}_{-0.27}$	0.97
NGC 1142 (D)	359^{+133}_{-117}	$1.3^{+2.8}_{-1.3}$	$0.80^{+1.04}_{-0.50}$	$0.69^{+0.32}_{-0.21}$	$1.81^{+0.19}_{-0.09}$	$0.25^{+0.14}_{-0.12}$	0.19	$6.6^{+8.5}_{-6.1}$	72^{+39}_{-13}	$0.98^{+0.01}_{-0.02}$	$1.26^{+0.26}_{-0.20}$	0.86
LEDA 170194 (C)	26^{+229}_{-10}	$0.0^{+0.73}_{-0.0}$	$0.27^{+0.27}_{-0.09}$	$1.15^{+0.11}_{-0.67}$	$1.73^{+0.08}_{-0.10}$	$5.7^{+2.2}_{-5.7}$	3.65	$0.5^{+0.5}_{-0.4}$	$5.7^{+0.6}_{-0.5}$	$0.96^{+0.02}_{-0.05}$	$0.13^{+0.13}_{-1.00}$	0.80

not resemble normal distributions. The values of the Compton parameter form a relatively broad peak centered around 0.8, overimposed by a narrow peak around $y = 1.1$. Using the results of different spectral model options we have checked how the main parameters change with the model complexity. Since the distributions for all fitted models are asymmetric, to compare them we computed the median values instead of the standard averages. These numbers are shown in Table 4. Although the sample is small we can draw some conclusions. In general, more realistic models (B,C,D) lead to a smaller scatter of the kT_e and R values, reducing the high-value tail of their distributions. Except for R in the case of model Ba, the median values for all parameters are comparable. As shown in the lower part of Table 4, the median values for all four parameters are quite similar for Seyferts type 1, 1.5 and 2.

To understand the systematic differences between the results of models Ba and B we have studied the plots showing

each spectral component separately. Figure 4 illustrates such an analysis for 4U 0517+17. The bias introduced by model Ba can be explained as follows. If in the host galaxy there exists an ionized, partially covering absorber besides the fully covering absorber, a simple absorption model alone cannot reproduce a slight modification of the absorbed continuum due to the partial absorption. This modification present in model B is shown in Fig. 4 with the magenta curve. The missing partial absorber component in model Ba is counterbalanced by the fit of a strengthened reflection component. At the same time the fitted plasma temperature and Compton parameter can be altered due to the adjustment of several spectral components to match the strong reflection component.

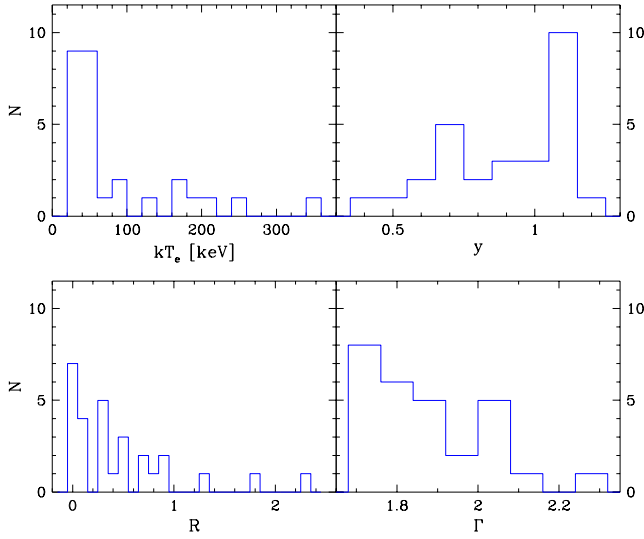


Figure 3. Distributions of the best model values of the plasma temperature kT_e , Compton parameter y , Compton reflection R and spectral index Γ .

Table 4. Median values of four main parameters of the continuum model for the studied sample. The medians were computed for different model options and for the best selected model for the whole sample and for three Seyfert types. The uncertainties were computed as the lower and upper quartiles.

Model option	kT_e [keV]	y	Γ	R
A	64^{+136}_{-24}	$0.83^{+0.23}_{-0.16}$	$1.89^{+0.10}_{-0.10}$	$0.34^{+0.53}_{-0.18}$
Ba	52^{+265}_{-16}	$1.00^{+0.15}_{-0.20}$	$1.77^{+0.09}_{-0.05}$	$0.81^{+0.77}_{-0.28}$
B	50^{+135}_{-16}	$0.92^{+0.15}_{-0.21}$	$1.83^{+0.15}_{-0.06}$	$0.29^{+0.35}_{-0.18}$
C	49^{+105}_{-12}	$0.89^{+0.20}_{-0.14}$	$1.88^{+0.12}_{-0.12}$	$0.25^{+0.37}_{-0.23}$
D	51^{+96}_{-16}	$0.90^{+0.18}_{-0.19}$	$1.82^{+0.14}_{-0.06}$	$0.30^{+0.30}_{-0.28}$
Whole sample	48^{+57}_{-14}	$0.94^{+0.16}_{-0.22}$	$1.81^{+0.18}_{-0.05}$	$0.32^{+0.33}_{-0.28}$
Type 1	45^{+80}_{-11}	$0.94^{+0.15}_{-0.23}$	$1.85^{+0.17}_{-0.08}$	$0.33^{+0.24}_{-0.15}$
Type 1.5	44^{+70}_{-8}	$1.04^{+0.04}_{-0.32}$	$1.80^{+0.21}_{-0.03}$	$0.30^{+0.17}_{-0.17}$
Type 2	45^{+83}_{-29}	$0.93^{+0.18}_{-0.21}$	$1.80^{+0.15}_{-0.05}$	$0.32^{+0.46}_{-0.25}$

4.3 Bolometric luminosity

The bolometric luminosity is one of the most fundamental quantities characterizing radiation from a celestial object. In the case of AGN this is a particularly important parameter allowing to estimate the efficiency of the accretion process. An estimate of the bolometric luminosity is difficult when the spectral energy distribution is not sufficiently covered by measurements (e.g., UV and very soft X-ray emission) and contamination arising from the host galaxy can influence the measurement of the AGN core flux. Thus, usually one uses some substitute based on the data from a given band. The X-ray band is preferred for AGN, as there is a negligible contamination from the rest of the host galaxy and the X-ray flux correlates well with the flux emitted by the AGN in the other energy bands (e.g., radio, infrared and optical). Commonly applied are luminosity estimates based either on the medium energy X-rays, e.g., that have been proposed by Marconi et al. (2004) for

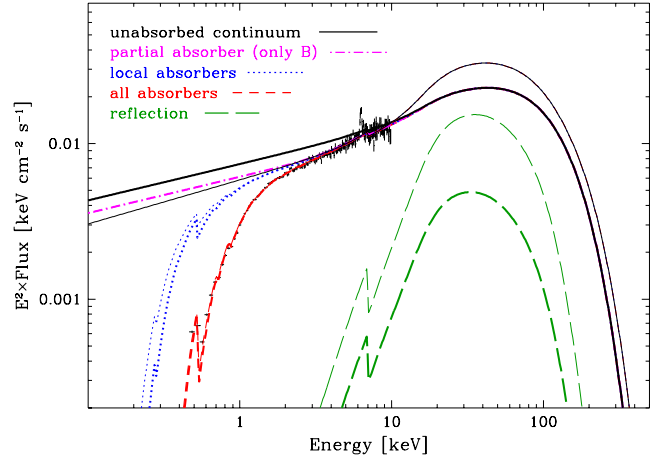


Figure 4. Spectral components fitted to the *XMM-Newton* spectrum of 4U 0517+17 with the models B (thick lines) and Ba (thin lines). Modifications of the primary continuum by all, local to the host galaxy and partially covering absorbers (only model B) are shown. The Compton reflection component is strengthened in model Ba.

the 2–10 keV band, or on the hard X-rays, e.g., 20–100 keV band chosen by Beckmann et al. (2009). On the other hand, there are attempts to determine the bolometric luminosity from the entire spectral energy distribution (SED) seen for a given source (e.g., Vasudevan et al. 2010). Unfortunately, even very careful analysis of that type can suffer from some missing information when a large number of objects is considered. Very often this missing information pertains to the soft γ -ray emission above 100 keV, where some AGN radiate a significant fraction.

For the sake of taking into account the entire emission in the X-ray and γ -ray bands, we have chosen yet another estimate of the bolometric luminosity L_{bol} for our sample. Namely, we assumed that the luminosity integrated in the 1 eV – 1 MeV band for the best-fitting unabsorbed model corresponds to half of the bolometric luminosity. Our L_{bol} values are listed in Table 5 together with the luminosities computed for the seed photons and Comptonized continuum components. The last column of Table 5 presents our estimates of the average Eddington ratio λ_E for each object. To compute λ_E we used the relation $L_{\text{Edd}} = 1.3 \times 10^{38} M_{\text{BH}}$ ergs s^{−1} for the Eddington accretion luminosity, where the BH mass is given in solar mass units.

In order to investigate the accuracy of our estimates, we collected various luminosity estimates from the literature, based on different measurements and methods. In addition, we also computed the bolometric luminosity using the 2–10 keV and 20–100 keV band fluxes integrated for the best-fitting model and the formulae of Marconi et al. (2004) and Beckmann et al. (2009), respectively. All those luminosity estimates are plotted in Figure 5 as a function of our L_{bol} estimates. The dashed line in this figure indicates the one-to-one relation between the two luminosity estimates. Clearly, our estimates do correspond well to the average luminosity estimates for a given object, as determined with the other methods. Only for the low and high luminosity ends of the sample we observe a small departure from this trend. To quantify those deviations we fitted a line to the literature data in a function of our L_{bol} , assuming that all literature

data are affected by the same error. The resulting relation is

$$\log L_{\text{bol, literature}} = (0.84 \pm 0.05) \times \log L_{\text{bol}} + (7.1 \pm 2.3), \quad (2)$$

the corresponding curve is plotted in Fig. 5 with a solid line.

An assumption of equal uncertainty for all literature data is the simplest solution in situation when majority of those data lack the uncertainty estimate. We have found that to obtain reduced $\chi^2 = 1$ for the above fit, a 0.4 dex error has to be set for each $\log L_{\text{bol, literature}}$ value. For one-to-one relation the reduced $\chi^2 = 1.07$. The differences between the two lines shown in Fig. 5 are much smaller than the scatter of the luminosity estimates seen in Fig 5. Therefore, for the studied sample we keep our simple choice for L_{bol} estimate. We would like to stress that our choice was proved to be valid only for this particular AGN sample. A general relation similar to Eq. 2 should be verified with a larger AGN sample and with a reliable estimate of the literature data uncertainties.

Our L_{bol} luminosity estimate is twice the luminosity of the high temperature plasma. Interestingly, in a recent study of the luminosity of a sample of local Seyfert galaxies it was found that the corona and accretion disc intrinsically radiate approximately equal power (Sazonov et al. 2012). There are several other sources of the AGN radiation: jet, torus and outflows (e.g., those forming a broad emission line region, BLR). However, when a conversion of the gravitational energy into radiation is considered for a given accretion system, radiation reprocessed in torus should not be taken into account in the energy budget. The bolometric luminosity estimates of Vasudevan et al. (2010) and Sazonov et al. (2012) follow these lines, considering only a primary disc and plasma radiation. Since the disc emission in the UV and soft X-ray bands is hardly observed directly due to absorption, their estimate of the disc luminosity is indirect, based on the infrared emission from the torus illuminated by the disc. We used a simpler way to estimate the disc luminosity but our results are very similar to those of Khorunzhev et al. (2012), used by Sazonov et al. (2012). For 17 common objects we obtain a line with a slope 0.95 and total $\chi^2 = 6.6$, assuming 0.4 dex uncertainty.

Whereas the emission in the infrared band is the torus reprocessed emission from the disc and plasma region, a radio emission induced by the jet kinetic energy can be important for the direct accretion power budget. Radio emission from the radio-quiet Seyferts is negligible compared to the disc and plasma emission. Among radio-loud objects in our sample only Cygnus A emits a large fraction of its energy in the radio band, approximately about 20%, according to the spectral energy distribution (SED) data collected in the NASA Extragalactic database (NED). For the rest of the radio-loud objects in our sample similar estimate gives at most 1% for 3C 390.3 and 3C 120, whereas for 3C 111 it is well below 1%. Thus, only for Cygnus A there can be missing some fraction of the jet luminosity but our L_{bol} estimate (the most luminous object in Fig. 5) do not show too low luminosity compared to the other results.

Table 5. Logarithms of bolometric luminosities (in ergs s^{-1}) and the Eddington ratio λ_E for studied Seyferts computed for the selected best-fitting model. L_{seed} - luminosity of the seed photons component, L_{Comp} - luminosity of the Comptonized component of the spectrum integrated in the 1 eV – 1 MeV band, L_{bol} - bolometric luminosity of the AGN, computed as a doubled value of the total model luminosity in the 1 eV – 1 MeV band.

Object	L_{seed}	L_{Comp}	L_{bol}	λ_E
IC 4329A	43.65	44.67	44.98	0.070
IGR J21247+5058	43.24	44.52	44.85	0.086
GRS 1734-292	43.77	44.55	44.91	0.0072
NGC 4593	42.37	43.60	43.90	0.045
4U 0517+17	42.81	44.03	44.38	0.122
Akn 120	44.67	45.08	45.40	0.128
ESO 141-55	44.17	44.79	45.26	0.352
3C 111	44.15	45.16	45.49	0.217
NGC 4151	42.24	43.51	43.84	0.020
MCG+8-11-11	43.94	44.80	45.10	0.092
Mrk 509	43.65	44.78	45.35	0.114
4U 1344-60	42.70	43.87	44.23	0.028
3C 120	44.64	45.13	45.45	0.352
NGC 6814	41.73	43.04	43.34	0.012
3C 390.3	44.04	45.20	45.50	0.072
MCG-6-30-15	43.28	43.76	44.09	0.131
NGC 4388	42.79	44.05	44.36	0.157
NGC 2110	42.70	43.89	44.25	0.0084
NGC 4507	42.75	44.12	44.42	0.039
MCG-5-23-16	43.45	44.11	44.45	0.077
NGC 5506	42.98	43.83	44.15	0.053
Cygnus A	44.74	45.49	45.82	0.020
NGC 5252	43.27	44.54	44.84	0.018
ESO 103-35	43.55	44.23	44.57	0.176
NGC 788	42.80	43.98	44.29	0.053
NGC 6300	41.59	42.55	43.01	0.018
NGC 1142	43.51	44.48	44.89	0.024
LEDA 170194	43.26	44.55	44.85	0.014

4.4 Compton amplification and Compton reflection

There are several other parameters characterizing the AGN accreting system that can be derived from the parameters of the models fitted to the X/ γ spectra. One of them is the Compton amplification factor A_C , computed as the ratio of the Comptonized plus seed photon fluxes to the seed photon flux. We have computed A_C values using the model fluxes of the Comptonized and black-body components, integrated in the 1 eV – 1 MeV band. In Figure 6 we present the spectral index Γ plotted against A_C . This dependence can be well approximated by a power-law formula. As can be seen, our results agree particularly well with the approximation found for AGN by Malzac et al. (2001), based on simulations of a dynamic corona atop an accretion disc.

A detailed study of the correlations between our results and other parameters characterizing accretion systems at the centre of Seyfert galaxies is out of the scope of the present paper. The only dependence we want to refer to is the correlation between the Compton reflection and photon index found for Seyferts and BH binaries in many previous studies (e.g., those based on the Ginga data, Zdziarski et al. 1999). Figure 7 presents our Γ - R data compared with the

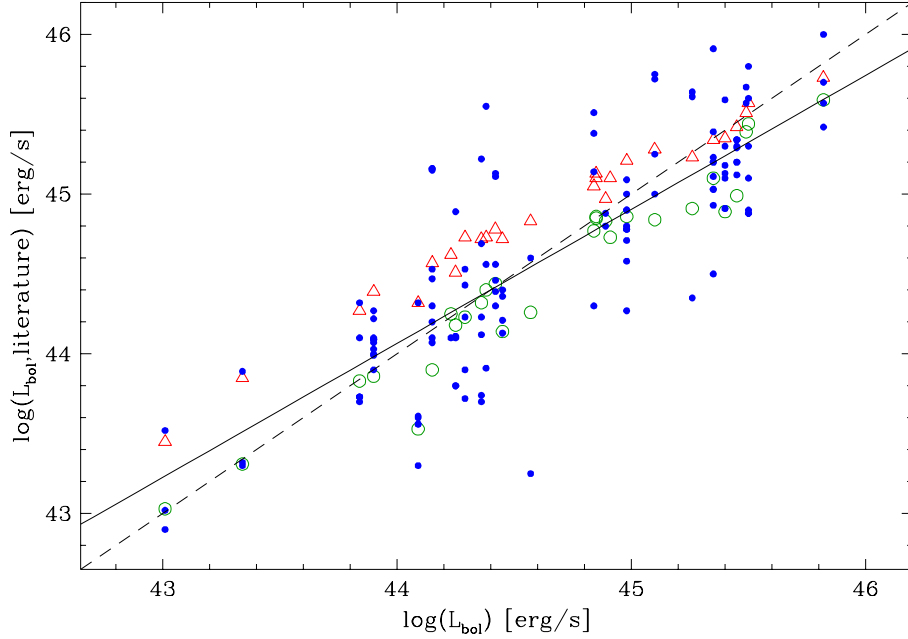


Figure 5. Bolometric luminosity estimates for the studied AGN sample. Values taken from the literature are plotted against our bolometric luminosity measure, $L_{\text{bol}} = 2 \times L(1 \text{ eV} - 1 \text{ MeV})$. The data, shown with dots, come from: Khorunzhev et al. (2012), Winter et al. (2012), Vasudevan et al. (2009, 2010), Woo & Urry (2002), Wang & Zhang (2007), Middleton et al. (2008), Chitnis et al. (2009), Zhang (2011), Zhou et al. (2010), Raimundo et al. (2012), Marinucci et al. (2012), Bian & Gu (2007) and Alonso-Herrero et al. (2011). Two other estimates are: $6 \times L(20 \text{ keV} - 100 \text{ keV})$, Beckmann et al. (2009) (circles), Marconi et al. (2004) formula using the 2–10 keV luminosity (triangles). Solid line shows the linear fit to the literature data. Dashed line is the equality line.

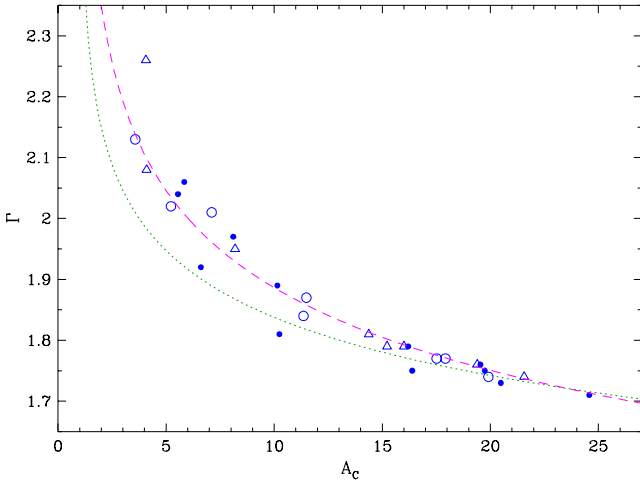


Figure 6. Photon index Γ as a function of the Compton amplification parameter A_C (circles - Sy 1, triangles - Sy 1.5, dots - Sy 2). Dotted and dashed lines show the power-law approximation of the $\Gamma(A_C)$ dependence found by Beloborodov (1999) and Malzac et al. (2001), respectively.

relation found in Zdziarski et al. (1999) (this relation takes into account an internal correlation of these two parameters in the PEXRAV model used for Ginga spectra). Although the broad-band spectral analysis presented here allows for a better determination of both Γ and R , the true correlation can be suppressed due to the averaging of data collected during various spectral states. This explains a less prominent R - Γ correlation than that seen for the short exposure time observations reported in Zdziarski et al. (1999).

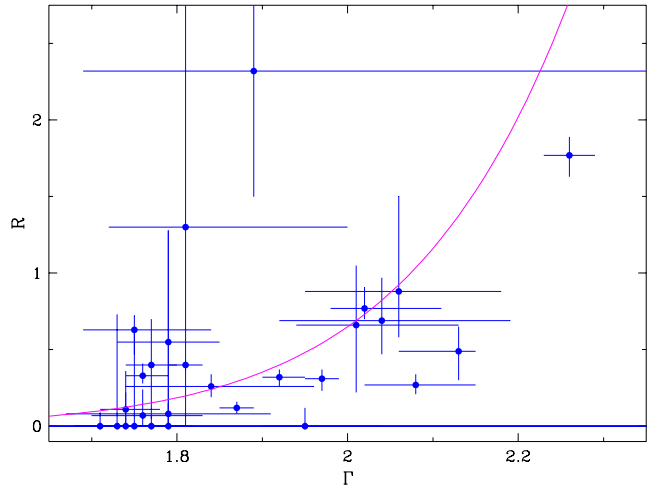


Figure 7. Reflection strength R as a function of the photon index Γ determined for our sample. Line shows the power-law approximation of the $R(\Gamma)$ dependence found by Zdziarski et al. (1999).

5 DISCUSSION

5.1 Comparison with previously published results

5.1.1 Comptonization model, CGRO and BeppoSAX samples

First we compare our results with those quoted in Sec. 1, namely diverging kT_e estimates based on CGRO (Zdziarski et al. 2000) and BeppoSAX (Petrucci et al. 2001) observations. Analysis of the CGRO data is compatible with ours thanks to the application of the same Comptonization

model. The *CGRO*/OSSE spectra of Type 1 (17 objects) and Type 2 (10 objects) nuclei were stacked separately and fitted with a fixed $R = 0.75$. Best-fit Compton parameter and plasma temperature are: $0.89_{-0.52}^{+0.36}$ and 69_{-28}^{+134} keV for Sy 1, and $1.09_{-0.41}^{+0.29}$ and 84_{-31}^{+101} keV for Sy 2. Uncertainty of those estimates is quite large, despite the high quality of the OSSE spectra, due to the lower limit of the energy band at 50 keV. The agreement with our results, presented in Table 4 and Fig. 3, is very good. Thus our analysis of the Seyfert spectra is fully consistent with the results obtained for the OSSE detector.

Analysis done with the *BeppoSAX* spectra (Petrucci et al. 2001) was limited to only six sources, among them IC 4329A, NGC 4151, ESO 141-55 and Mrk 509 from our sample. The authors used the anisotropic Comptonization model of Haardt (1993) assuming a slab geometry for the corona above the disc. The slab geometry gives typically kT_e values similar to those derived for the spherical plasma and y values about two times smaller (see e.g., Lubiński et al. (2010)). The kT_e values quoted in Petrucci et al. (2001) are in the range between 170 and 315 keV, with quite small uncertainties (typically 5–30 keV). Such a high accuracy is rather surprising because the sensitivity of the *BeppoSAX*/PDS detector was only slightly higher than that of ISGRI and the *BeppoSAX* exposure times were about ten times shorter than the ISGRI exposure times. The Compton reflection estimated with the *BeppoSAX* spectra is also quite large, typically close to $R = 1$ with an error of about 10–30 per cent. All the objects with high kT_e estimates based on the *BeppoSAX* data belong to the low kT_e group of our analysis, with the $R \ll 1$. Therefore, there is a substantial discrepancy between these two analyses. Higher kT_e estimates based on the *BeppoSAX* spectra can be explained by the fact that the best-fitting model are driven by the low-energy spectra from the LECS and MECS detectors, having many channels with relatively small errors, whereas the PDS spectra are quite scarce above 50 keV. Our suggestion is based on inspection of figure 2 in Petrucci et al. (2001), where the high-energy tails of the IC 4329A and especially NGC 4151 spectra are softer than the plotted model. Taking into account the quality of the *BeppoSAX* spectra above 100 keV it seems that the computed kT_e uncertainties are underestimated in situation where the best-fitting kT_e is much higher than the upper energy limit of the fitted spectrum. In turn, the *BeppoSAX* R values are increased due to a higher plasma temperature making the reflected component flatter.

5.1.2 Phenomenological model, large samples

A detailed comparison with all previously published results of the spectral modelling done already with various X/ γ spectra of the studied sample is out of scope of the present paper. We limit this analysis to several recent papers presenting the results obtained for large samples of Seyfert galaxies and several papers on individual objects. Spectra of all Seyfert samples discussed here were analysed with a phenomenological model in the form of a power-law with a high energy cut-off E_C (XSPEC model PEXRAV). Hard X-ray spectra fitted by those groups were taken with *BeppoSAX*/PDS + low-energy spectra from *BeppoSAX*/MECS (Dadina 2007), *RXTE*/HEXTE + *RXTE*/PCA (Rivers et al. 2013),

Swift/BAT + *Suzaku* and *XMM-Newton* (Winter et al. 2012) and *INTEGRAL*/ISGRI: + *INTEGRAL*/JEMX (Beckmann et al. 2009), + *XMM-Newton*, *Chandra*, *ASCA* and *Swift*/XRT (Molina et al. 2009), + *XMM-Newton* (De Rosa et al. 2012) and + *XMM-Newton* and *Swift*/BAT (Malizia et al. 2014). All those analyses applied a fully covering neutral absorber, whereas a partial/ionized absorption component was added only by Dadina (2007), Molina et al. (2009) and Malizia et al. (2014).

In Figure 8 we compare the results of the studies quoted above with our results for Γ and R , respectively. The largest AGN sample considered here is the *INTEGRAL* catalogue of Beckmann et al. (2009); their analysis is simplified and suffers also from a lack of high-quality low-energy spectra (*INTEGRAL*/JEMX has rather limited sensitivity). Therefore, the obtained Γ values are quite scattered (see Fig. 8, panel (a)), and the authors did not fit a Compton reflection component. An analysis of the *BeppoSAX* spectra by Dadina (2007) provided Γ results consistent with ours within $\Delta\Gamma = \pm 0.1$ but the R values are usually larger than ours (panels (b)). For the rest of the Γ comparisons (panels c–f) there is a relatively large scatter of values observed. On average, in all cases (except for Winter et al. (2012)) our spectra seem to be systematically softer, in agreement with the results of the tests presented in Sec. 4.1: harder spectra are fitted with simpler absorption model Ba.

Interestingly, our results show the narrowest range of the fitted Γ values, with a sharp cut-off at low values. The shape of the Γ distribution is the result of the y and kT_e distributions, both with a relatively narrow main peak. When the spectra are fitted with the COMPPS model, the spectral slope is a result of Comptonization of seed photons. Since the seed photon distribution must occupy some region within optical, UV and soft X-ray bands, the Comptonized spectra cannot be too hard because otherwise the normalization of the seed photon distribution will become too small to produce a sufficient number of Compton upscattered photons for a given optical depth of the plasma. An additional regulation of the spectral slope comes from the fitted kT_e , due to the dependence of the Comptonization efficiency on the energy gain per one scattering. Therefore, Comptonization model provides physical limitations on the spectral slope, when compared to the phenomenological models where the Γ parameter is completely free.

Comparison of the fitted R values shown in Fig. 8 confirms our conclusion that simpler models produce, on average, a larger Compton reflection. Only the results of the *RXTE* data analysis by Rivers et al. (2013) are roughly consistent with our results. We have also compared the high-energy cut-off values E_C fitted with the PEXRAV model with our kT_e results, using two relations $kT_e = E_C/2$ for $\tau \lesssim 1$ and $kT_e = E_C/3$ for $\tau \gg 1$ (Petrucci et al. 2001). A vast majority of the plasma temperature estimates based on the exponential cut-off model appeared to be larger than the kT_e results obtained by us with the Comptonization model. This difference can be explained again by less complex models applied in the analysis of larger samples. By less complexity of the model we mean several factors: a simpler absorption model, an exponential cut-off instead a Comptonized continuum (which decreases more rapidly at high energy, see Sec. 5.4) and a neglected variability of the low-energy spectra with respect to the spectral slope and absorption.

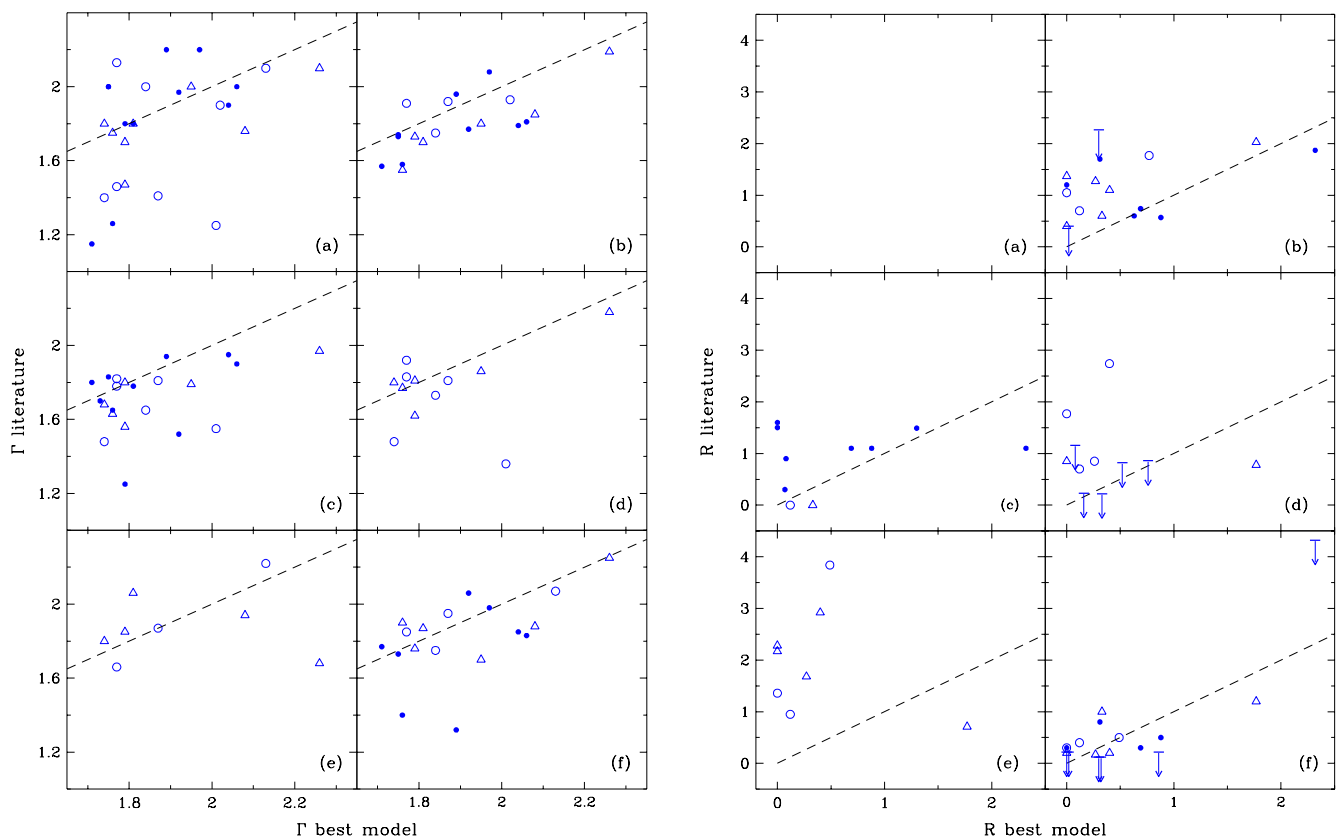


Figure 8. Left: Comparison of the photon index Γ determined in several recent analyses with our Γ results. Right: Comparison of the Compton reflection strength R determined in several recent analyses with our R results (there is no R data in Beckmann et al. (2009), panel a). Data were taken from: (a) - Beckmann et al. (2009), (b) - Dadina (2007), (c) - Malizia et al. (2014); De Rosa et al. (2012), (d) - Molina et al. (2009), (e) - Winter et al. (2012), (f) - Rivers et al. (2013). Object types: circles - Sy 1, triangles - Sy 1.5, dots - Sy 2. The dashed lines show the equality lines.

Ricci et al. (2011) presented an analysis of the average spectra extracted for several classes of AGN from the stacked *INTEGRAL*/ISGRI images. Interestingly, they determined with the PEXRAV model an average photon index of $\Gamma = 1.8$, i.e., the same as our sample median. Their mean $E_C \lesssim 200$ keV is also compatible with the arithmetic mean $kT_e \approx 80$ keV for our sample, assuming $kT_e - E_C$ conversion factor between 2 and 3. Moreover, for the three Seyfert groups (Sy 1, Sy 1.5, Sy 2) with $N_H < 10^{23} \text{ cm}^{-2}$ they found upper limits for R in the range 0.4–0.5, i.e., lower than usually reported and again compatible with our R distribution median.

5.1.3 Short-term observations, individual objects

Studies discussed so far in this Section were done for samples of AGN and the spectral properties were derived for hard X-ray spectra collected over several years, usually accompanied by the low-energy spectra with shorter exposure time. Only analyses of the *BeppoSAX* (Dadina 2007) and *RXTE* (Rivers et al. 2013) were done for contemporary low- and high-energy spectra. Thus it was desirable to compare our results with some results based on shorter but roughly contemporary broad-band observations done for individual objects. Although there can be some differences due to shorter sampling time, many of such observations

were analysed with the Comptonization models, allowing us to directly compare the kT_e values.

Since the sensitivity of the *NuSTAR* satellite in the 10–50 keV band is much higher than the sensitivity of any other satellite operating so far, we considered here mainly the results of the *NuSTAR* observations. Contemporary *Suzaku* and *NuSTAR* spectra of IC 4329A in a flux state near its long-time average were analyzed in detail by Brenneman et al. (2014). Their plasma temperature and optical depth values, 50_{-3}^{+6} keV and 2.3 ± 0.2 , respectively, found with the COMPTT Comptonization model agree well with our results shown in Table 3. Similar overall agreement is found also for the high-temperature object Akn 120, which was observed simultaneously by *NuSTAR* and *XMM-Newton* (Matt et al. 2014). The energy coverage of the *NuSTAR* detectors ($\lesssim 80$ keV) precluded more precise determination of the high-energy cut-off value in this case. Both continuum models, PEXRAV and COMPPS, applied to fit the cut-off gave only a rough estimate, $E_C > 340$ keV and kT_e in between 110 and 210 keV, respectively. Whereas $R = 0.26 \pm 0.08$ found by Matt et al. (2014) with the PEXRAV model is marginally consistent with our result (0.5 ± 0.2), their $\Gamma = 1.79 \pm 0.03$ is much smaller than our estimate ($2.13_{-0.07}^{+0.02}$). This discrepancy can be explained by a variability of the emission and a difference in the absorption model: there was no warm ab-

sorber found for the *NuSTAR* observation whereas our best fit needed a modest ionized, partly covering absorption.

Another object from our sample with recently analysed *NuSTAR* spectra is NGC 2110 (Marinucci et al. 2015). The *NuSTAR* spectra were fitted with a simple absorption model, accompanied by either a phenomenological or Comptonization model for the main continuum component. Comptonization model **COMP**TT resulted in $kT_e = 190 \pm 130$ keV, i.e., close to our value of 230 keV. We note a large discrepancy for the Compton reflection strength, with the upper limit estimated at $R = 0.14$ for both *NuSTAR* observations fitted with a cut-off power-law + reflection model, whereas our R value is quite large, around 0.6. Our fit with model **Ba** gave a similar R value, thus the discrepancy is rather not related to a different absorption model. The **PEXRAV** model accompanied by three partially covering absorbers was used to analyse two *Suzaku* observations of NGC 2110, with no reflection detected (Rivers et al. 2014). Thus, a possible explanation of the different R values can be different continuum model used in our and other analyses. In addition, our *INTEGRAL* NGC 2110 spectra cover the period before the brightening of the source in 2012, whereas the two *NuSTAR* observations were performed in 2012 and 2013. There can be some change of the spectral properties of the source after unusual brightening. Indeed, when we added the recent *INTEGRAL* data extracting a new summed ISGRI spectrum, the preliminary fit resulted in much smaller $R \approx 0.25$.

Thanks to its excellent sensitivity the *NuSTAR* satellite will bring more interesting results for other objects from our sample, especially for those with a cut-off at low energy. Since *NuSTAR* observations are sampling the emission of a given source over a shorter time and less frequently, some difference in the results will always be expected. *INTEGRAL* is more suited for the studies of the average emission over long periods, thus both these missions well complement each other. But even for *INTEGRAL* we note clear differences for spectra taken over different periods. An example is Mrk 509, target of an extensive multi-mission observation campaign in 2009 (Kaastra et al. 2011). A spectral analysis with two Comptonizing, hot and warm, coronae revealed their temperature around 100 keV and 1 keV, respectively (Petrucchi et al. 2013). In our spectral analysis we modelled only the hot corona and found its $kT_e = 39^{+20}_{-9}$ keV. In order to clarify this difference we have fitted our model to the ISGRI spectrum extracted only for the 2009 campaign period, accompanied by contemporary *XMM-Newton* spectra. The best-fitting value for the plasma temperature $kT_e = 82^{+42}_{-33}$ keV is consistent with the value determined by Petrucci et al. (2013), although it is less accurate than the result obtained using all available spectra. When all spectral data from *INTEGRAL* are analyzed, the cut-off is clearly seen as shown in Fig. 2.

5.2 Plasma diagnosis

5.2.1 Geometry and seed photons

Contemporary models of the radiation processes in the accreting BH systems assume a hybrid, thermal plus non-thermal plasma (Belmont et al. 2008; Veledina et al. 2011). The non-thermal electrons are responsible for the synchrotron radiation cooling the plasma in addition to the

emission from the cold accretion disc. Based on the low values determined for both kT_e and R we propose a qualitative argument supporting the importance of the synchrotron cooling process. First, R with the median value around 0.3 indicates that the solid angle, covered by the accretion disc as seen from the plasma region, is relatively small, especially if one takes into account that some fraction of the reflection comes from the torus. Thus, if the disc and plasma are well separated spatially, we expect an even smaller solid angle under which the compact plasma region is seen from the disc. This means a reduced flux of the disc soft photons cooling the plasma. At the same time we observe low kT_e values for many low- R objects. Therefore, there should exist another mechanism cooling the plasma and the synchrotron self-absorption is a plausible explanation. The range of Eddington ratios where the Comptonization of the synchrotron photons can be dominant, was suggested to be within 0.0001–0.01 (Malzac 2012). The majority of the low- kT_e and low- R objects of our sample accrete close to that range, below $\lambda_E = 0.05$.

We have estimated the relative Compton parameter variability, $\Delta y/y$, where Δy was computed as the standard deviation for the arithmetic mean. For this we used y values fitted to the low-energy spectra with the best model selected by the Akaike test among those allowing for the spectral slope variation (option B or D). Except for NGC 4388, NGC 788 and NGC 1142 all object exhibit $\Delta y/y \leq 20$ per cent. Such a stability of the Compton parameter can be explained by the synchrotron boiler model, assuming a complete absorption of the synchrotron emission within the corona. Figure 3 of Ghisellini et al. (1998), showing a dependence of kT_e and y on the compactness of the injected non-thermal electrons, presents the y values in a range very similar to that found for our sample, supporting the synchrotron self-Compton model. The plasma temperature shown in that figure is too high for a large range of compactness values but it can be shifted towards lower values when the other cooling radiation (disc photons) is taken into account. Recent studies of the synchrotron self-Compton model confirmed the stability of the spectral slope against variations of many parameters such as magnetization, optical depth or Eddington ratio (Veledina et al. 2011). Nevertheless, models including the Comptonization of the disc photons can also be adjusted to get a stable spectral slope (Stern et al. 1995), although in this case the geometry of the plasma and the disc should allow for their close interaction. Thus, taking into account that our kT_e and R results point towards a separation of these two regions, the synchrotron regulation appears highly probable.

The fact that the R - Γ correlation holds even for the mean values of these parameters indicates that both cooling processes are important. The self-regulating effect of the synchrotron self-Compton model can be smaller if some fraction of synchrotron emission escapes from the plasma. An extension of the Veledina et al. (2011) model was proposed to explain a complicated connection between the variability of the optical/infrared (OIR) and X-ray emission of the BH systems (Veledina et al. 2013). In this model most of the OIR emission originates in a hot flow, closer to the BH than the truncated accretion disc. The source of this emission is the synchrotron radiation of non-thermal electron population. Such a model, with the changing inner radius of the

disc, offers essentially the same explanation for the R - Γ correlation (Poutanen & Veledina 2014) as that presented in Zdziarski et al. (1999).

Non-thermal electrons are needed to get a substantial flux of synchrotron photons, ensuring an efficient plasma cooling down to the observed temperatures (especially if the magnetic field is relatively weak). As can be seen from the ISGRI spectra of Seyferts (e.g., Fig. 1), we are still far from the possibility of observing the high-energy power-law tails, such as those found in the spectra of Galactic BH binaries (McConnell et al. 2000; Wardziński et al. 2002; Zdziarski et al. 2012). Therefore, a direct measurement of the non-thermal electrons fraction will not be possible for Seyferts with any current and, presumably, any near-future satellite.

5.2.2 Plasma radiation power

Our estimate of the bolometric luminosity is based on an assumption that both the plasma and the disc emit approximately half of the total AGN radiation power. As mentioned in Sec. 5, Sazonov et al. (2012) found a similar equality of the powers generated by the disc and by the hot corona. Their disc luminosity estimate is based on the mid-infrared luminosity of the torus, where the disc emission is reprocessed. For the hot corona they assumed that 30 per cent of its total flux is emitted in the 17–60 keV band. The 30 per cent fraction corresponds to the cut-off power-law model with $\Gamma = 1.7$ and $E_C = 200$ keV, consistent with the average spectrum of the local AGN sample studied by Sazonov et al. (2008). The ratio of the observed disc luminosity to the corona luminosity found by Sazonov et al. (2012) is ≈ 2 . Then, taking into account a reprocessing of the corona emission in the disc, they conclude that the intrinsic luminosities of the disc and the corona are roughly equal. Since L_{bol} computed by us is related to the observed, not intrinsic corona flux, there is a discrepancy between Sazonov et al. (2012) and our results. The lower corona luminosity found by Sazonov et al. (2012) can be explained by their assumption that their L_{HX} luminosity determined for the 17–60 keV band corresponds to ≈ 30 per cent of the total corona luminosity. As can be checked, this assumption is valid if their model is integrated in a limited range between 2 and 300 keV, whereas for the 0.001–1000 keV band L_{HX} corresponds to only ≈ 21 per cent of the corona luminosity. Therefore, compared to our results their corona luminosity is underestimated by a factor ≈ 1.5 . This explains why our L_{bol} estimate gives good results under an assumption of equal disc and corona luminosities.

Sazonov et al. (2012) do not propose an explanation for the equal powers of the disc and corona emission. Since they interpret their other results within a scenario of the compact corona seen at small solid angle from the disc, any disc-corona interaction mechanism leading to the emitted power equality can be insufficient. For the alternative scenario, assuming an extended corona above the disc, there was such mechanism proposed for the Galactic black holes (Schnittman et al. 2013). Based on the magnetohydrodynamic simulations results they conclude ‘the MHD turbulence in an accretion disc can lead to dissipation outside the disc’s photosphere strong enough to power hard X-ray emission comparable in luminosity to the disc’s thermal lu-

minosity’. However, this type of model cannot explain the small Compton reflection determined for Seyfert galaxies as well as positive lags between the hard X-ray and optical/UV emission. In addition, similarly to the other models assuming a corona extended above the disc, it predicts too steep X-ray spectra in the 2–10 keV band, with Γ well above 2 (see fig. 12 in Schnittman et al. 2013).

5.3 Comparison with Galactic BH binaries

The temperatures of the Comptonizing plasma found for Galactic black hole binaries observed in the hard state are typically in the range between 70 and 100 keV, whereas during the soft state they are in the 10–40 keV range (Malzac 2012). Both soft and hard state BHB and the low-temperature AGN samples are far too small to judge whether there is a significant difference between their mean kT_e values. The other parameter values, like $\Gamma < 2$ or $\lambda_{\text{Edd}} < 0.05$, computed for the majority of our sample, correspond rather to the values typical for the hard state BHB. Moreover, as stated in Malzac (2012), the only model consistent with data for soft state BHB is the accretion disc extended down to the last stable orbit and small active coronal regions above the disc. Such a model will result in R close to 1, not consistent with our results. This discrepancy can be solved by applying a dynamic plasma model, forming mildly relativistic outflows (Beloborodov 1999) but this in turn demands a strong magnetic field needed for fast energy dissipation in the corona. Therefore, our results, consistent with the scenario of plasma and disc being well separated, support the hard state BHB - Seyfert correspondence.

5.4 Consequences for CXB studies

The X/γ template spectra of AGN are one of the most important elements of the population synthesis models aiming at explaining the CXB spectrum. Since there are many other constraints and effects to be taken into account in such studies, for simplicity the template spectra are commonly approximated with an absorbed, exponentially cut-off power-law model, accompanied by a Compton reflection (e.g., Treister et al. 2009; Ueda et al. 2014). However, an approximation of the high-energy cut-off of the Comptonized spectrum with the exponential cut-off is known to be poor, especially for the spectra with $kT_e \lesssim 100$ keV (see fig. 5 in Zdziarski et al. 2003). To illustrate this effect again we have plotted in Fig. 9 three Comptonization models together with the corresponding phenomenological models approximating them. Two Comptonization spectra were computed for $kT_e = 50$ keV, i.e., close to our sample median, the third spectrum is for $kT_e = 250$ keV, i.e., slightly above the highest more accurately determined temperature within our sample (NGC 2110). Cut-off energy E_C was adjusted according to the relation quoted in Sec. 5.1. As can be seen in panel (a) of Fig. 9, for high kT_e the exponential cut-off with $E_C = 2kT_e$ relatively well approximates the Comptonization cut-off.

For the low kT_e regime the situation is much worse: for both $kT_e = 50$ and 100 keV the $E_C = 3kT_e$ relation does not work. This is due to the fact that the exponential cut-off changes the shape of the spectrum already in the energy band well below kT_e , whereas the Comptonized

spectrum cut-off is much sharper and appears close to the cut-off energy. In consequence, to recover the sharper cut-off the exponential cut-off models fitted to the spectra lead to the spectral models harder than those fitted with the Comptonization model. We tested this effect applying the PEXRAV model to our spectra of NGC 4151. When we fix E_C at 160 keV (equal to the $kT_e = 53$ keV multiplied by 3), the other parameters are strongly altered, with $\Gamma \approx 1.55$ and $R \approx 0.45$ instead of 1.75 and 0.33, respectively, found with the Comptonization model. Also the parameters of the partial absorber component were changed due to the need to adjust to the harder continuum.

Our sample, although not very large, is the largest Seyfert sample modelled with the complex physical model. We found that the plasma emitting in the X/ γ band is relatively cool, with only a small fraction of objects showing kT_e above 100 keV. This fact has to be taken into account in CXB modelling, where the template spectra are used to model the total emission from the Seyfert galaxies, dominating the AGN population. Contemporary synthesis models assume E_C in the 150–400 keV range. In panel (b) of Fig. 9 we show several examples of the template spectra, compared with the Comptonization model corresponding to our median kT_e , y and R values. The spectra used by Ballantyne et al. (2006) ($E_C = 375$ keV), Gilli et al. (2007) ($E_C = 200$ keV) and Ueda et al. (2014) ($E_C = 300$ keV) are more concave below the peak due to the stronger Compton reflection assumed, $R = 1$. All template spectra are less steep above the peak than our spectrum, with a considerable emission above 200 keV. The rightmost dash-dotted spectrum corresponding to the upper quartile of our kT_e distribution, i.e. 105 keV, definitely overpredicts the high-energy emission and forms too broad peak to be consistent with the CXB spectrum. This is the result of the fact that our sample is not homogeneous. In future population studies the high- kT_e objects should be considered separately, provided that this subsample will be enlarged.

Any quantitative analysis of the CXB template spectra is out of the scope of the present paper. Definitely, a substantial change in the template model will affect the population synthesis model, altering its results in many respects. If the low-temperature plasma is a common feature of not only local Seyferts, there will be several consequences expected. The most important will be the need to reduce the expected population of the heavily absorbed, so-called Compton-thick (CT) AGN. These objects, with $\log(N_H) > 24$ cm $^{-2}$, can be detected only in the hard X-ray domain, where the sensitivity of the contemporary observatories remains too low for a detection of more distant sources. Current hard X-ray surveys place the fraction of CT AGN among all local AGN in the range between 0 and 20 per cent (e.g., Beckmann et al. 2009; Burlon et al. 2011). The cumulated emission from CT AGN forms a relatively narrow peak (Gilli et al. 2007) at energy close to the CXB peak. Population synthesis models suggest the CT AGN fraction, corrected for the selection effect, in a wide range between 5 and 50 per cent (Akylas et al. 2012). If the typical Seyfert spectra are more peaked due to the lower high-energy cut-off than the template spectra used so far, there will be smaller population of CT AGN needed. The Compton reflection also contributes to the CXB peak. Although we found this component to be weaker than that assumed usually in the synthesis models, its role in form-

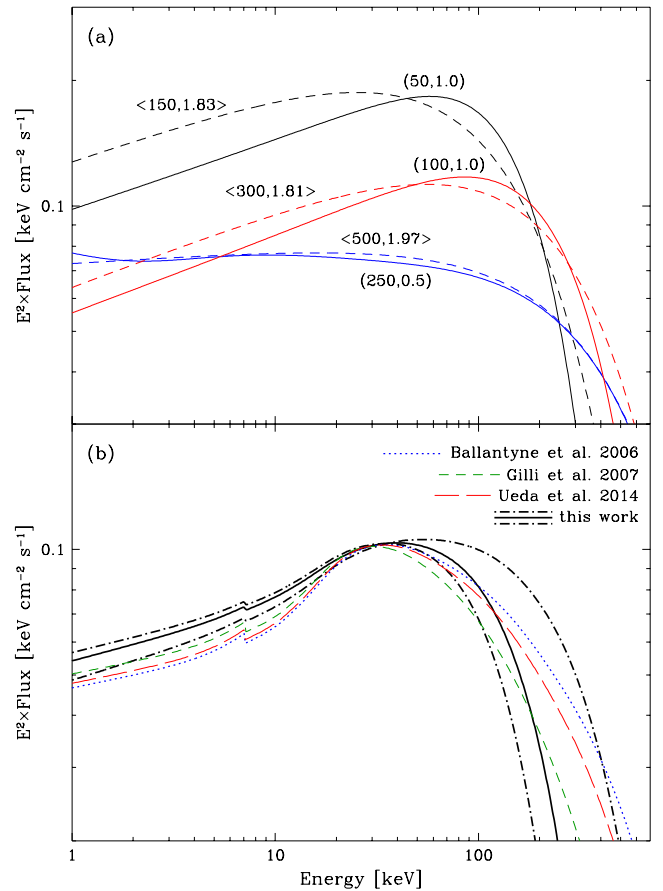


Figure 9. (a) Comparison between Comptonization model (COMPPS, solid lines) and exponentially cut-off power-law model (PEXRAV, dashed lines) approximating it. kT_e and y parameters of COMPPS models are given in round brackets, E_C and Γ parameters of PEXRAV models are given in angle brackets. Normalization is arbitrary, models do not include the Compton reflection component. (b) Examples of the PEXRAV template spectra used in modelling of the AGN population synthesis compared with the Comptonization spectrum corresponding to the median values of kT_e , y and R determined by us. The dash-dotted lines show models corresponding to the quartiles of the kT_e distribution determined by us. Spectra are normalized to the same level at 30 keV.

ing the peak will be reinforced due to its narrower shape after reprocessing a primary continuum emission with lower temperature (cf. Fig. 2).

The exponential cut-off template spectra shown in Fig. 9 are less steep at high energy than the Comptonization model spectrum. This will affect additionally the synthesis model results, in particular the CXB peak, weakening it due to the emission from distant, high-redshift AGN. The fact that models with large E_C reproduce the CXB spectrum in a wide energy range indicates that there is some emission needed at high energy, in excess to that coming from the low-temperature Seyferts. Taking this into account more advanced studies of the AGN population should be possible, aiming at identifying the sources of the high-energy emission. These can be some rare, high-temperature, radio-quiet Seyfert galaxies like Akn 120 and NGC 2110. However, the main candidates for the sources dominating 100–300 keV emission are presumably radio-loud AGN. Observa-

tions show that the fraction of the radio-loud objects among all AGN is at most several per cent (Best 2009). These objects are much stronger emitters above 100 keV than the Seyferts, being well fitted with the cut-off power-law models with $E_C > 300$ keV, e.g., Cen A (Beckmann et al. 2011) and 3C 273 (Esposito et al. 2015). Future population synthesis models can attempt to disentangle the CXB components related to the radio-quiet and radio-loud AGN.

6 CONCLUSIONS

We have analysed the summed, long-exposure time spectra of 28 Seyfert nuclei, collected over the 2002–2012 period by the *INTEGRAL*/ISGRI detector. These hard X-ray/soft γ -ray data were fitted together with all contemporary medium X-ray spectra taken with the *XMM-Newton*, *Suzaku* and *RXTE* satellites. We have applied a complex physical spectral model including a Comptonized continuum, a Compton reflection component and two absorption components corresponding to a neutral and to an ionized, partially covering absorption media.

To take into account the spectral variability of the low-energy spectra, various options of the model were fitted, including variable spectral slope and variable absorption. As the result of a massive spectral fit campaign we have obtained a set of relatively precise average values of many physical parameters for the largest Seyfert sample so far studied with such an elaborate model.

A mean temperature of the electron plasma was found to be $26 \leq kT_e \leq 62$ keV for a majority (19 among 28) of the studied objects. The rest of the sample exhibits mean temperatures $80 \leq kT_e \leq 360$ keV. The distribution of the mean Compton parameter is bimodal, with a narrow peak around $y = 1.1$ and a broad peak around $y = 0.8$, the latter corresponding to almost all high-temperature objects. Mean values of the photon index Γ , derived from the mean y and kT_e values, occupy a narrow range between 1.7 and 2.1, except for two objects. Compared to the previous analyses, we found much weaker Compton reflection strength, with a vast majority of the R values well below 1, and only three objects showing $R > 1$.

Regardless the small size of subsamples we found very similar median values of the kT_e , y and R parameters for the three types of Seyfert galaxies. On the other hand, radio-loud objects are characterized by higher kT_e and lower y than the radio-quiet objects.

Our results are in agreement with an emerging paradigm of the hard X-ray source in Seyfert nuclei being compact and localized at the centre of the system, separated geometrically from the accretion disc. The narrow range of observed y values points toward a quite similar plasma geometry within the low-temperature subsample. On the other hand, high-temperature objects show a larger range of the Compton parameter, related presumably to considerable differences of the system geometry and/or plasma heating and cooling mechanisms.

Reduced irradiation of the disc by the plasma photons and vice versa, together with the low plasma temperatures observed, indicates that there should be another process, besides the disc emission, needed to explain an efficient plasma cooling. The most probable effect is the plasma synchrotron

emission, within scenarios postulated by the recent hybrid Comptonization models.

We have found that the integrated X-ray and γ -ray luminosity provides a very good estimate of half of the total accretion luminosity of the Seyfert galaxies. This finding confirms a recent observation that the radiation emitted by the plasma region and the radiation of the accretion disc are approximately equal for these sources.

Compared with the results of the X-ray spectral analysis obtained for Galactic BH binaries, our results support an analogy between BHBs in the hard state and bright Seyfert galaxies.

The low typical kT_e we found for the Seyferts' plasma implies that the template spectra adopted in AGN population synthesis models should be revised. The most important consequence of a shifted high-energy cut-off will be a considerably smaller fraction of the Compton-thick AGN needed to explain the peak of the CXB spectrum. For the same reason, a population of radio-loud AGN will be needed to balance the reduced emission of radio-quiet AGN in the 100–300 keV band.

ACKNOWLEDGMENTS

PL and AAZ have been supported by the Polish NCN grants 2012/04/M/ST9/00780 and UMO-2014/13/B/ST9/00570. We thank the reviewer for his/her thorough review and highly appreciate the comments and suggestions, which significantly contributed to improving the quality of the publication. We used data from the High Energy Astrophysics Science Archive Research Center, and from the NASA/IPAC Extragalactic Database. We acknowledge the usage of the HyperLeda database (<http://leda.univ-lyon1.fr>). Most of the massive computations was done using the NCAC cluster in Toruń, excellently maintained by Jerzy Borkowski.

REFERENCES

- Abramowicz M. A., Chen X., Kato S., Lasota J., Regev O., 1995, *ApJL*, **438**, L37
- Akaike H., 1973, in Petrov B. N., Csaki F., eds, 2nd International Symposium on Information Theory. pp 267–281
- Akylas A., Georgakakis A., Georgantopoulos I., Brightman M., Nandra K., 2012, *A&A*, **546**, A98
- Alon-Herrero A., et al., 2011, *ApJ*, **736**, 82
- Anders E., Ebihara M., 1982, *Geochim. Cosmochim. Acta*, **46**, 2363
- Arnaud K. A., 1996, in Jacoby G. H., Barnes J., eds, Astronomical Society of the Pacific Conference Series Vol. 101, Astronomical Data Analysis Software and Systems V. pp 17–+
- Awaki H., Murakami H., Leighly K. M., Matsumoto C., Hayashida K., Grupe D., 2005, *ApJ*, **632**, 793
- Ballantyne D. R., Everett J. E., Murray N., 2006, *ApJ*, **639**, 740
- Beckmann V., Shrader C. R., 2012, *Active Galactic Nuclei*. Wiley-VCH
- Beckmann V., et al., 2009, *A&A*, **505**, 417
- Beckmann V., Jean P., Lubiński P., Soldi S., Terrier R., 2011, *A&A*, **531**, A70
- Belmont R., Malzac J., Marcowith A., 2008, *Mem. S.A.It.*, **79**, 228
- Beloborodov A. M., 1999, in Poutanen J., Svensson R., eds, Astronomical Society of the Pacific Conference Series Vol. 161, High Energy Processes in Accreting Black Holes. p. 295 ([arXiv:astro-ph/9901108](https://arxiv.org/abs/astro-ph/9901108))

- Bentz M. C., et al., 2006, *ApJ*, **651**, 775
- Best P. N., 2009, *Astronomische Nachrichten*, **330**, 184
- Bian W., Gu Q., 2007, *ApJ*, **657**, 159
- Bian W., Zhao Y., 2003, *MNRAS*, **343**, 164
- Brenneman L. W., et al., 2014, *ApJ*, **788**, 61
- Burlon D., Ajello M., Greiner J., Comastri A., Merloni A., Gehrels N., 2011, *ApJ*, **728**, 58
- Chatterjee R., et al., 2011, *ApJ*, **734**, 43
- Chitnis V. R., Pendharkar J. K., Bose D., Agrawal V. K., Rao A. R., Misra R., 2009, *ApJ*, **698**, 1207
- Courvoisier T. J.-L., et al., 2003, *A&A*, **411**, L53
- Czerny B., Nikolajuk M., Piasecki M., Kuraszewicz J., 2001, *MNRAS*, **325**, 865
- Dadina M., 2007, *A&A*, **461**, 1209
- De Rosa A., et al., 2012, *MNRAS*, **420**, 2087
- Denney K. D., et al., 2006, *ApJ*, **653**, 152
- Esposito V., Walter R., Jean P., Tramacere A., Türler M., Läh-
teenmäki A., Tornikoski M., 2015, *A&A*, **576**, A122
- Garcia-Rissmann A., Vega L. R., Asari N. V., Cid Fernandes R.,
Schmitt H., González Delgado R. M., Storchi-Bergmann T.,
2005, *MNRAS*, **359**, 765
- Gehrels N., et al., 2004, *ApJ*, **611**, 1005
- Ghisellini G., Haardt F., Svensson R., 1998, *MNRAS*, **297**, 348
- Gierliński M., 2000, PhD thesis, N. Copernicus Astronomical Cen-
ter, Warsaw
- Gilli R., Comastri A., Hasinger G., 2007, *A&A*, **463**, 79
- Górecki A., Wilczewski W., 1984, *Acta Astronomica*, **34**, 141
- Graham A. W., 2008, *ApJ*, **680**, 143
- Gu Q., Melnick J., Cid Fernandes R., Kunth D., Terlevich E.,
Terlevich R., 2006, *MNRAS*, **366**, 480
- Gültekin K., et al., 2009, *ApJ*, **698**, 198
- Haardt F., 1993, *ApJ*, **413**, 680
- Harrison F. A., et al., 2013, *ApJ*, **770**, 103
- Kaastra J. S., et al., 2011, *A&A*, **534**, A36
- Kalberla P. M. W., Burton W. B., Hartmann D., Arnal E. M.,
Bajaja E., Morras R., Pöppel W. G. L., 2005, *A&A*, **440**, 775
- Khorunzhev G. A., Sazonov S. Y., Burenin R. A., Tkachenko
A. Y., 2012, *Astronomy Letters*, **38**, 475
- Kuo C. Y., et al., 2011, *ApJ*, **727**, 20
- Lebrun F., et al., 2003, *A&A*, **411**, L141
- Lubiński P., Zdziarski A. A., Walter R., Paltani S., Beckmann V.,
Soldi S., Ferrigno C., Courvoisier T., 2010, *MNRAS*, **408**, 1851
- Magdziarz P., Zdziarski A. A., 1995, *MNRAS*, **273**, 837
- Malizia A., Molina M., Bassani L., Stephen J. B., Bazzano A.,
Ubertini P., Bird A. J., 2014, *ApJL*, **782**, L25
- Malzac J., 2012, *International Journal of Modern Physics Conference Series*, **8**, 73
- Malzac J., Beloborodov A. M., Poutanen J., 2001, *MNRAS*,
326, 417
- Marchesini D., Celotti A., Ferrarese L., 2004, *MNRAS*, **351**, 733
- Marconi A., Risaliti G., Gilli R., Hunt L. K., Maiolino R., Salvati
M., 2004, *MNRAS*, **351**, 169
- Marconi A., Axon D. J., Maiolino R., Nagao T., Pastorini G.,
Pietrini P., Robinson A., Torricelli G., 2008, *ApJ*, **678**, 693
- Marinucci A., Bianchi S., Nicastro F., Matt G., Goulding A. D.,
2012, *ApJ*, **748**, 130
- Marinucci A., et al., 2015, *MNRAS*, **447**, 160
- Markowitz A., 2009, *ApJ*, **698**, 1740
- Matt G., et al., 2014, *MNRAS*, **439**, 3016
- McConnell M. L., et al., 2000, *ApJ*, **543**, 928
- McHardy I. M., Gunn K. F., Uttley P., Goad M. R., 2005,
MNRAS, **359**, 1469
- Middleton M., Done C., Schurch N., 2008, *MNRAS*, **383**, 1501
- Mitsuda K., et al., 1984, *PASJ*, **36**, 741
- Mitsuda K., et al., 2007, *PASJ*, **59**, 1
- Molina M., et al., 2009, *MNRAS*, **399**, 1293
- Morrison R., McCammon D., 1983, *ApJ*, **270**, 119
- Mushotzky R. F., Cowie L. L., Barger A. J., Arnaud K. A., 2000,
Nature, **404**, 459
- Nandra K., Pounds K. A., 1994, *MNRAS*, **268**, 405
- Nicastro F., Martocchia A., Matt G., 2003, *ApJL*, **589**, L13
- Paturel G., Petit C., Prugniel P., Theureau G., Rousseau J.,
Brouty M., Dubois P., Cambrésy L., 2003, *A&A*, **412**, 45
- Peterson B. M., et al., 2004, *ApJ*, **613**, 682
- Petrucchi P. O., 2008, *Mem. S.A.It.*, **79**, 118
- Petrucchi P. O., et al., 2001, *ApJ*, **556**, 716
- Petrucchi P.-O., et al., 2013, *A&A*, **549**, A73
- Poutanen J., Svensson R., 1996, *ApJ*, **470**, 249
- Poutanen J., Veledina A., 2014, *SSRv*, **183**, 61
- Protassov R., van Dyk D. A., Connors A., Kashyap V. L., Siemigi-
nowska A., 2002, *ApJ*, **571**, 545
- Puccetti S., Fiore F., Risaliti G., Capalbi M., Elvis M., Nicastro
F., 2007, *MNRAS*, **377**, 607
- Raimundo S. I., Fabian A. C., Vasudevan R. V., Gandhi P., Wu
J., 2012, *MNRAS*, **419**, 2529
- Reeves J., Done C., Pounds K., Terashima Y., Hayashida K.,
Anabuki N., Uchino M., Turner M., 2008, *MNRAS*, **385**, L108
- Reynolds C. S., 2014, *SSRv*, **183**, 277
- Ricci C., Walter R., Courvoisier T. J.-L., Paltani S., 2011, *A&A*,
532, A102
- Rivers E., Markowitz A., Rothschild R., 2013, *ApJ*, **772**, 114
- Rivers E., et al., 2014, *ApJ*, **786**, 126
- Rybicki G. B., Lightman A. P., 1979, *Radiative processes in as-
trophysics*. New York, Wiley-Interscience, 1979. 393 p.
- Sazonov S., Krivonos R., Revnivtsev M., Churazov E., Sunyaev
R., 2008, *A&A*, **482**, 517
- Sazonov S., et al., 2012, *ApJ*, **757**, 181
- Schnittman J. D., Krolik J. H., Noble S. C., 2013, *ApJ*, **769**, 156
- Stalin C. S., Jeyakumar S., Coziol R., Pawase R. S., Thakur S. S.,
2011, *MNRAS*, **416**, 225
- Stern B. E., Poutanen J., Svensson R., Sikora M., Begelman
M. C., 1995, *ApJL*, **449**, L13+
- Sugiura N., 1978, *Communications in Statistics - Theory and Methods*,
7, 13
- Svensson R., 1999, in Poutanen J., Svensson R., eds, *Astro-
nomical Society of the Pacific Conference Series Vol. 161*,
High Energy Processes in Accreting Black Holes. p. 361
([arXiv:astro-ph/9902204](https://arxiv.org/abs/astro-ph/9902204))
- Tazaki F., Ueda Y., Ishino Y., Eguchi S., Isobe N., Terashima Y.,
Mushotzky R. F., 2010, *ApJ*, **721**, 1340
- Treister E., Urry C. M., Virani S., 2009, *ApJ*, **696**, 110
- Tremaine S., et al., 2002, *ApJ*, **574**, 740
- Turner T. J., Miller L., 2009, *A&ARv*, **17**, 47
- Ueda Y., Akiyama M., Hasinger G., Miyaji T., Watson M. G.,
2014, *ApJ*, **786**, 104
- Uttley P., McHardy I. M., 2005, *MNRAS*, **363**, 586
- Vasudevan R. V., Mushotzky R. F., Winter L. M., Fabian A. C.,
2009, *MNRAS*, **399**, 1553
- Vasudevan R. V., Fabian A. C., Gandhi P., Winter L. M.,
Mushotzky R. F., 2010, *MNRAS*, **402**, 1081
- Veledina A., Vurm I., Poutanen J., 2011, *MNRAS*, **414**, 3330
- Veledina A., Poutanen J., Vurm I., 2013, *MNRAS*, **430**, 3196
- Wandel A., 2002, *ApJ*, **565**, 762
- Wang J.-M., Zhang E.-P., 2007, *ApJ*, **660**, 1072
- Wang J., Mao Y. F., Wei J. Y., 2009, *AJ*, **137**, 3388
- Wardziński G., Zdziarski A. A., Gierliński M., Grove J. E., Jahoda
K., Johnson W. N., 2002, *MNRAS*, **337**, 829
- Winkler C., et al., 2003, *A&A*, **411**, L1
- Winter L. M., Mushotzky R. F., Reynolds C. S., Tueller J., 2009,
ApJ, **690**, 1322
- Winter L. M., Lewis K. T., Koss M., Veilleux S., Keeney B.,
Mushotzky R. F., 2010, *ApJ*, **710**, 503
- Winter L. M., Veilleux S., McKernan B., Kallman T. R., 2012,
ApJ, **745**, 107

- Wit E., Heuvel E. v. d., Romeijn J.-W., 2012, *Statistica Neerlandica*, 66, 217
- Woo J.-H., Urry C. M., 2002, *ApJ*, 579, 530
- Woo J.-H., et al., 2010, *ApJ*, 716, 269
- Yuan F., 2001, *MNRAS*, 324, 119
- Zdziarski A. A., Johnson W. N., Done C., Smith D., McNaron-Brown K., 1995, *ApJL*, 438, L63
- Zdziarski A. A., Lubiński P., Smith D. A., 1999, *MNRAS*, 303, L11
- Zdziarski A. A., Poutanen J., Johnson W. N., 2000, *ApJ*, 542, 703
- Zdziarski A. A., Lubiński P., Gilfanov M., Revnivtsev M., 2003, *MNRAS*, 342, 355
- Zdziarski A. A., Lubiński P., Sikora M., 2012, *MNRAS*, 423, 663
- Zhang Y.-H., 2011, *ApJ*, 726, 21
- Zhou X.-L., Wang J.-M., 2005, *ApJL*, 618, L83
- Zhou X.-L., Zhang S.-N., Wang D.-X., Zhu L., 2010, *ApJ*, 710, 16

APPENDIX A: ESTIMATE OF THE BLACK HOLE MASS

There are various methods used to determine the mass of supermassive black holes residing in the center of normal and active galaxy nuclei. Each of those methods has some limitations. For example, the reverberation mapping, probably the most robust technique besides that applying a water maser emission, can suffer from the radiation pressure affecting the BLR size estimate (Marconi et al. 2008). Indeed, the reverberation-based mass estimates are usually smaller than the values derived with the other methods. In addition, reverberation mapping of the broad line region cannot be used for absorbed objects where this region is obscured. To reduce a role of the limitations of different methods we decided to compute a weighted mean of the BH masses found in the literature together with our estimates based on the stellar velocity dispersion data.

The numbers used for the mean computation are shown in the Table A1. In this Table we adopted method's symbols defined in the second *INTEGRAL* AGN catalogue (Beckmann et al. 2009): 'R' - reverberation mapping, 'SO' - indirect estimate of σ_* from the O III line width, 'CL' - size of the BLR from the continuum luminosity, 'LL' - size of the broad line region from the H β line luminosity, 'KM' - K-band stellar magnitude, 'S' - a direct measure of the stellar velocity dispersion, 'X' - X-ray power spectral density, 'M' - water maser, 'B' - bulge luminosity, 'N' - narrow line region size from the H β line.

Our estimate uses the average values of stellar velocity dispersion σ_* taken from the Hyper Leda database (Paturel et al. 2003), except for MCG-6-30-15, NGC 4507, NGC 6300 and NGC 1142 where we used σ_* values from Garcia-Rissmann et al. 2005 and for NGC 5506 and ESO 103-55 from Gu et al. 2006. The velocity dispersions were converted into M_{BH} values using the Tremaine et al. 2002 formula. We tried also a more recent formula of Gültekin et al. 2009 but the logarithms of BH masses were almost the same (difference ≤ 0.1) as for the Tremaine et al. 2002 equation. There are several other estimates using method 'S' in the Table A1, however, we have checked that there were other σ_* data used. In the second column of Table A1 there are literature values compiled in the Beckmann et al. 2009 catalogue, with the reference given. The other literature numbers are taken from the papers listed in the caption of Table A1. We have checked those data to avoid a double use of the same value. If for a given method there are at least two numbers used for the mean computation, they are based on either a different approach for the same observational data or a different data set. For example, Vasudevan et al. 2010 and Winter et al. 2012 estimates, based on the K-band stellar magnitudes from the Two Micron All Sky Survey (2MASS), were obtained with different corrections and different formulas to convert them into BH mass values. Thus, we treated these two estimates as independent measures.

Black hole masses determined with the reverberation mapping shown in Table A1 were taken from Peterson et al. 2004 unless there was a newer, more precise result published. In the case of Winter et al. 2012 we quote the original numbers from the paper for Sy 1 and Sy 1.5 objects, whereas for Sy 2 we used Winter et al. 2009 data and a correction found

in Winter et al. 2010. Several values shown in the Table A1, put into square brackets, were skipped during the mean computation. These are three numbers from Wang & Zhang 2007 included in the Beckmann et al. 2009 data, two catalogue values for NGC 1142 and LEDA 170194 where the Winter et al. 2009 values were corrected by us (fifth column of the Table A1) and our estimate for GRS 1734-292 included already in the Beckmann et al. 2009 catalogue. We also excluded the Winter et al. 2010 value for IGR J21247+5058 because their extinction correction for the continuum emission at 5100 Å seems too large (Tazaki et al. 2010). At last, the 'Catalogue' value for MCG-6-30-15 was excluded too, because this is a mean value for different methods computed by Uttley & M^cHardy 2005. In this case we used the original Uttley & M^cHardy 2005 values derived with the X-ray variability method, quoted in the last column of Table A1.

The weighted mean of the BH masses was computed for the logarithm values, with the uncertainty for different methods expressed in dex units. For the 'Catalogue' we used the original errors quoted in Beckmann et al. 2009. For the other data we applied the uncertainty estimates from the middle of the uncertainty limits suggested in Beckmann et al. 2009. Thus, the errors of $\log(M_{\text{BH}})$ adopted by us were: 0.1 dex for method 'M', 0.2 dex for methods 'K' and 'R', 0.3 dex for method 'S', 0.5 dex for methods 'B', 'CL', 'KM', 'LL', and 0.7 dex for methods 'N' and 'X'. As a check we tried also an arithmetic mean which produced the results quite similar to the weighted mean.

Table A1. Various estimates of the masses of supermassive black holes for the sample of studied Seyfert galaxies. This work: M_{BH} derived from the average values of stellar velocity dispersion. “Catalogue” is the second *INTEGRAL* AGN catalog (Beckmann et al. 2009) from which we adopted the codes of various methods applied for the M_{BH} estimate (see the text). The references quoted are: (1) Winter et al. 2010, (2) Winter et al. 2009, 2012, (3) Vasudevan et al. 2010, (4) Bian & Zhao 2003, (5) Wang & Zhang 2007, (6) Khorunzhev et al. 2012, (7) Wang et al. 2009, (8) Peterson et al. 2004, (9) Markowitz 2009, (10) Tazaki et al. 2010, (11) Denney et al. 2006, (12) Wandel 2002, (13) Woo et al. 2010, (14) Stalin et al. 2011, (15) Marchesini et al. 2004, (16) Chatterjee et al. 2011, (17) Bentz et al. 2006, (18) Woo & Urry 2002, (19) Uttley & McHardy 2005, (20) McHardy et al. 2005, (21) Middleton et al. 2008, (22) Bian & Gu 2007, (23) Kuo et al. 2011, (24) Nicastro et al. 2003, (25) Zhou & Wang 2005, (26) Graham 2008, (27) Czerny et al. 2001, (28) Awaki et al. 2005. Values in square brackets were not used (see the text).

Object	$\log(M_{\text{BH}}) [M_{\odot}]$												Others (reference)
	Reference Method	This work S	Catalogue	(1) CL	(2) KM	(3) KM	(4) CL	(5) LL	(5) SO	(6) KM	(6) LL	(7) LL	
IC 4329A		8.41	7.00(R,8)	—	8.19	8.29	7.45	7.42	7.89	7.98	—	—	8.11(X+B,9)
IGR J21247+5058		—	—	[6.58]	—	—	—	—	—	—	—	—	7.80(CL+LL,10)
GRS 1734-292		[8.94]	8.94(S)	—	—	—	—	—	—	—	—	—	
NGC 4593		8.11	6.99(R,11)	7.83	8.29	7.51	7.12	7.22	6.55	7.98	7.10	7.12	6.91(B,12), 6.97(S,13), 6.882(R,29)
4U 0517+17		7.39	—	—	—	—	—	7.20	6.88	—	7.65	7.55	6.98(R,14)
Akn 120		8.26	8.18(R,8)	—	8.43	8.54	8.21	8.25	7.69	—	—	8.48	8.29(B,12), 8.15(S,13), 8.068(R,29)
ESO 141-55		7.62	7.10(SO,5)	—	—	—	—	7.91	[7.10]	—	—	—	
3C 111		7.10	9.56(B,15)	8.54	—	—	—	—	—	—	9.08	8.33	8.26(LL,16)
NGC 4151		6.97	7.66(R,17)	7.07	7.27	—	7.24	7.31	7.44	7.61	7.67	7.49	7.08(B,12), 7.64(S,13), 7.555(R,29)
MCG+8-11-11		6.37	8.06(SO,5)	8.07	—	8.17	7.18	7.89	[8.06]	—	—	7.60	
Mrk 509		—	8.16(R,8)	—	8.26	8.56	7.70	7.66	7.80	8.15	8.22	7.47	7.98(B,13), 9.049(R,29)
4U 1344-60		7.89	—	—	—	7.44	—	—	—	—	—	—	
3C 120		7.86	7.74(R,8)	—	8.23	8.35	6.85	—	—	—	—	—	8.13(S,18), 7.49(B,12), 7.72(S,13), 7.745(R,29)
NGC 6814		7.12	7.08(CL,4)	—	7.78	—	6.95	—	—	7.53	6.91	6.95	7.28(CL,18), 7.25(S,13), 7.038(R,29)
3C 390.3		8.64	8.46(R,8)	—	8.19	8.35	8.51	—	—	—	9.61	9.13	8.59(B,12), 8.44(S,13), 8.638(R,29)
MCG-6-30-15		6.87	[6.65](X,19)	—	6.91	7.25	6.19	—	—	7.26	—	—	6.46(X,20), 6.81(SO,21)
NGC 4388		6.90	7.22(S,22)	—	8.20	7.07	—	—	8.16	7.20	—	—	6.93(M,23), 8.54(B,24)
NGC 2110		8.55	8.30(S,4)	—	7.92	7.40	—	—	7.96	—	—	—	
NGC 4507		7.63	7.58(S,22)	—	8.04	7.70	—	—	6.42	7.81	—	—	8.26(B,24)
MCG-5-23-16		7.94	6.29(SO,5)	—	7.24	—	—	—	[6.29]	7.28	—	—	7.85(N,25)
NGC 5506		6.88	6.65(S,22)	—	7.36	7.67	—	—	7.46	7.68	—	—	8.00(B,24)
Cygnus A		—	9.41(K,26)	—	—	—	—	—	—	—	—	—	
NGC 5252		8.09	8.98(K,26)	—	8.32	—	—	—	7.56	—	—	—	8.56(B,24)
ESO 103-35		7.15	7.14(X,27)	—	7.32	7.30	—	—	—	—	—	—	
NGC 788		7.53	7.51(S,22)	—	8.18	7.39	—	—	6.04	7.92	—	—	
NGC 6300		6.94	5.45(X,28)	—	—	>6.7	—	—	—	7.59	—	—	
NGC 1142		8.26	[9.36](KM,2)	—	9.11	7.98	—	—	—	8.48	—	—	
LEDA 170194		—	[8.88](KM,2)	—	8.58	—	—	—	—	—	—	—	

APPENDIX B: OBSERVATION LOG

Table B1. Details of the observations of the Seyferts sample done with *INTEGRAL* and other X-ray satellites. The last column shows the spectrum code within a spectral set used for a given object: I - *INTEGRAL*/ISGRI, X - *XMM-Newton*/EPIC pn, S - *Suzaku*/XIS, R - *RXTE*/PCA.

OBS ID	Start date	End date	Exposure [ks]	Spectrum
IC 4329A				
0030-0776	2002-12-21	2009-05-22	1774	I
0101040401	2001-01-31	2001-01-31	13.9	X2
0147440101	2003-08-06	2003-08-07	136.0	X1
702113010	2007-08-01	2007-08-01	25.4	S1
702113020	2007-08-06	2007-08-06	30.6	S2
702113030	2007-08-11	2007-08-11	26.9	S3
702113040	2007-08-16	2007-08-16	24.2	S4
702113050	2007-08-20	2007-08-17	24.0	S5
40153-01	2001-08-21	2001-08-27	52.6	R1
80152-03/04	2003-04-08	2004-02-26	140.0	R3
70148-01	2003-08-20	2003-08-23	60.8	R2
90154-01	2004-03-01	2007-07-17	58.4	R4
91138-01	2005-03-07	2007-08-07	57.6	R5
92108-01	2006-03-05	2007-06-26	65.1	R6
IGR J21247+5058				
0023-0806	2002-12-21	2009-05-22	5656	I
0306320101	2005-05-05	2005-05-05	11.8	X2
0306320201	2005-11-06	2005-11-07	27.8	X1
702027010	2007-04-16	2007-04-17	85.0	S1
GRS 1734-292				
0046-0849	2003-02-28	2009-09-28	15214	I
0550451501	2009-02-26	2009-02-26	17.9	X1
NGC 4593				
0028-0880	2003-01-05	2009-12-29	2962	I
0109970101	2000-07-02	2000-07-02	28.1	X2
0059830101	2002-06-23	2002-06-24	53.2	X1
702040010	2007-12-15	2007-12-16	118.8	S1
70145-02/03	2002-06-25	2002-07-10	174.3	R6
90160-02	2004-02-28	2006-02-09	151.7	R3
91140-04	2005-11-28	2006-01-31	174.1	R1
92113-02	2006-02-13	2007-06-28	154.7	R2
93127-05	2007-07-13	2008-12-25	126.5	R4
94127-05	2008-12-27	2009-12-30	121.0	R5
4U 0517+17				
0039-1328	2003-02-16	2013-08-29	2399	I
0502090501	2007-08-21	2007-08-22	61.9	X1
707029010	2013-02-28	2013-02-29	46.0	S1
Akn 120				
0041-0839	2003-02-14	2009-08-28	2209	I
0147190101	2003-08-24	2003-08-25	112.1	X1
702014010	2007-04-01	2007-04-02	100.9	S1
80160-03	2003-08-24	2006-12-28	113.7	R1
ESO 141-55				
0050-1262	2003-03-13	2013-02-13	979	I
0503750301	2007-10-09	2007-10-10	30.5	X3
0503750401	2007-10-10	2007-10-10	27.3	X4
0503750501	2007-10-12	2007-10-13	75.9	X2
0503750101	2007-10-30	2007-10-31	79.5	X1
3C 111				
0047-0837	2003-03-03	2009-08-23	2676	I
0065940101	2001-03-14	2001-03-15	44.8	X2
0552180101	2009-02-15	2009-02-17	124.6	X1
703034010	2008-08-22	2008-08-23	122.4	S1
90152-01	2004-03-01	2006-03-09	136.2	R1
91146-01	2005-03-31	2006-09-20	123.9	R2

Table B1 – continued

OBS ID	Start date	End date	Exposure [ks]	Spectrum
92102-01/04	2006-08-13	2007-05-04	221.0	R3
93137-01/03	2007-06-29	2008-12-25	136.3	R4
94137-01	2008-12-28	2009-12-30	58.6	R5
NGC 4151				
0036-1179	2003-01-29	2012-06-11	3236	I
0112310501	2000-12-21	2000-12-21	7.9	X1
0112310101	2000-12-21	2000-12-22	33.0	X1
0112830501	2000-12-22	2000-12-22	23.1	X1
0112830201	2000-12-22	2000-12-23	62.2	X1
0112830601	2000-12-23	2000-12-23	5.2	X1
0143500101	2003-05-25	2003-05-25	19.0	X2
0143500201	2003-05-26	2003-05-27	18.9	X2
0143500301	2003-05-27	2003-05-27	19.0	X3
0402660101	2006-05-16	2006-05-16	40.4	X4
0402660201	2006-11-29	2006-11-30	52.8	X5
0657840101	2011-05-11	2011-05-11	16.2	X6
0657840201	2011-06-12	2011-06-12	16.3	X7
0657840301	2011-11-25	2011-11-25	10.9	X8
0657840401	2011-12-09	2011-12-09	10.2	X9
0679780101	2012-05-13	2012-05-13	9.9	X10
0679780201	2012-06-10	2012-06-10	8.7	X11
701034010	2006-12-18	2006-12-20	125.0	S1
906006010	2011-11-17	2011-11-18	61.7	S2
906006020	2011-12-18	2011-12-19	60.6	S3
MCG+8-11-11				
0218-0966	2004-08-16	2010-09-12	1404	I
0201930201	2004-04-09	2004-04-10	38.4	X1
702112010	2007-09-17	2007-09-18	98.7	S1
00018	1996-01-22	1996-01-22	16.6	R1
Mrk 509				
0066-0867	2003-04-29	2009-11-20	1371	I
0306090201	2005-10-18	2005-10-19	85.9	X3
0306090301	2005-10-20	2005-10-20	47.1	X5
0306090401	2006-04-25	2006-04-25	69.9	X4
0601390201	2009-10-15	2009-10-16	60.9	X1
0601390301	2009-10-19	2009-10-20	63.8	X1
0601390501	2009-10-29	2009-10-30	60.9	X6
0601390601	2009-11-02	2009-11-03	62.8	X1
0601390701	2009-11-06	2009-11-07	63.1	X2
0601390901	2009-11-14	2009-11-15	60.9	X2
0601391001	2009-11-18	2009-11-18	65.5	X1
0601391101	2009-11-20	2009-11-21	62.8	X2
701093010	2006-04-25	2006-04-26	24.6	S1
701093020	2006-10-14	2006-10-14	25.9	S2
701093030	2006-11-15	2006-11-15	24.4	S3
701093040	2006-11-27	2006-11-27	33.1	S4
80157-01	2003-03-28	2006-07-29	190.6	R1
90147-01	2004-02-29	2006-07-25	169.6	R2
91129-01	2005-03-04	2006-07-19	79.2	R3
4U 1344-60				
0030-0850	2003-01-11	2009-09-30	5781	I
0092140101	2001-08-25	2001-08-25	36.9	X1
705058010	2011-01-11	2011-01-13	93.9	S1
3C 120				
0040-0839	2003-02-25	2009-08-28	1721	I
0109131101	2002-09-06	2002-09-06	12.6	X2
0152840101	2003-08-26	2003-08-27	133.8	X1
700001010	2006-02-09	2006-02-09	41.9	S1
700001020	2006-02-16	2006-02-17	41.6	S2
700001030	2006-02-23	2006-02-24	40.9	S3
700001040	2006-03-02	2006-03-03	40.9	S4

Table B1 – continued

OBS ID	Start date	End date	Exposure [ks]	Spectrum
70164-01	2002-03-01	2003-04-27	139.3	R1
80175-01	2003-04-29	2006-03-02	287.1	R2
90152-02	2004-06-24	2007-05-01	234.9	R3
91146-02	2005-06-24	2007-02-27	204.1	R4
92102-03	2006-11-15	2007-01-13	183.5	R5
NGC 6814				
0049-1041	2003-03-10	2011-04-25	3664	I
0550451801	2009-04-22	2009-04-22	32.3	X1
706032010	2011-11-02	2011-11-03	42.1	S1
30015-02	1998-05-18	1998-08-21	18.6	R1
3C 390.3				
0153-0829	2004-01-15	2009-07-30	1794	I
0203720201	2004-10-08	2004-10-09	70.4	X1
0203720301	2004-10-17	2004-10-17	52.8	X2
708034010	2013-05-24	2013-05-25	100.4	S1
50178-01	2000-03-03	2001-02-23	165.2	R1
90130-01	2005-01-12	2005-01-14	81.4	R2
MCG-6-30-15				
0030-0776	2003-01-11	2009-02-21	2174	I
0111570101	2000-07-11	2000-07-11	46.4	X1
0111570201	2000-07-11	2000-07-12	66.2	X2
0029740101	2001-07-31	2001-08-01	89.4	X3
0029740701	2001-08-02	2001-08-02	129.4	X4
0029740801	2001-08-04	2001-08-05	130.5	X5
100004010	2005-08-17	2005-08-17	46.7	S1
700007010	2006-01-09	2006-01-11	143.2	S2
700007020	2006-01-23	2006-01-24	98.5	S3
700007030	2006-01-27	2006-01-29	96.7	S4
80154-03	2003-06-08	2005-02-18	125.0	R1
91140-10	2005-03-07	2007-05-05	59.0	R2
92113-06	2006-03-05	2007-06-26	68.8	R3
93127-15/17	2007-05-19	2009-02-27	166.3	R4
94341-02	2009-03-03	2009-12-28	48.8	R5
NGC 4388				
0028-1012	2003-01-05	2011-01-27	4815	I
0110930701	2002-12-12	2002-12-12	12.0	X2
0675140101	2011-06-17	2011-06-18	61.4	X1
800017010	2005-12-24	2005-12-25	123.6	S1
NGC 2110				
0051-1035	2003-03-16	2011-04-06	1736	I
0145670101	2003-03-05	2003-03-06	59.6	X1
100024010	2005-09-16	2005-09-17	101.7	S1
30233-01	1997-12-07	1998-08-31	166.8	R1
80159-01	2003-03-05	2003-03-06	13.7	R2
NGC 4507				
0048-0776	2003-03-07	2009-02-21	1600	I
0006220201	2001-01-04	2001-01-05	46.2	X1
0653870201	2010-06-24	2010-06-24	19.9	X2
0653870301	2010-07-03	2010-07-03	16.9	X3
0653870401	2010-07-13	2010-07-14	16.9	X4
0653870501	2010-07-23	2010-07-23	16.9	X5
702048010	2007-12-20	2007-12-21	103.6	S1
10325-02	1996-02-24	1996-03-10	128.6	R1
80162-02-01	2003-06-25	2003-06-26	8.2	R2

Table B1 – continued

OBS ID	Start date	End date	Exposure [ks]	Spectrum
MCG-05-23-016				
0028-0770	2003-01-05	2009-02-03	839	I
0112830401	2001-12-01	2001-12-02	24.9	X2
0302850201	2005-12-08	2005-12-10	131.7	X1
700002010	2005-12-07	2005-12-09	95.7	S1
10307-01	1996-04-24	1997-01-10	145.8	R1
91703-14	2005-12-09	2005-12-09	12.8	R2
NGC 5506				
0095-0768	2003-07-24	2009-01-27	1479	I
0201830201	2004-07-11	2004-07-11	21.6	X1
0201830301	2004-07-14	2004-07-15	20.4	X2
0201830401	2004-07-22	2004-07-22	22.0	X3
0201830501	2004-08-07	2004-08-07	20.4	X4
0554170201	2008-07-27	2008-07-28	90.9	X5
0554170101	2009-01-02	2009-01-04	88.9	X6
701030010	2006-08-08	2006-08-09	47.8	S1
701030020	2006-08-11	2006-08-12	53.3	S2
701030030	2007-01-31	2007-01-31	57.4	S3
60133-02	2001-03-02	2002-05-20	136.9	R1
90145-01	2004-07-11	2004-08-08	30.5	R2
Cygnus A				
0022-0806	2002-12-18	2009-05-22	5614	I
0302800101	2005-10-14	2005-10-14	22.5	X1
0302800201	2005-10-16	2005-10-16	18.8	X2
803050010	2008-11-15	2008-11-16	44.7	S1
NGC 5252				
0028-1256	2003-01-05	2013-01-26	3674	I
0152940101	2003-07-18	2003-07-18	67.3	X1
707028010	2012-12-26	2012-12-27	50.3	S1
ESO 103-35				
0047-1030	2003-03-03	2011-03-21	1090	I
0109130601	2002-03-15	2002-03-15	12.9	X1
703031010	2008-10-22	2008-10-23	91.4	S1
20324-01	1997-04-11	1997-11-14	131.6	R1
NGC 788				
0098-0701	2003-08-02	2008-07-11	2136	I
0601740201	2010-01-15	2010-01-16	35.4	X1
703032010	2008-07-13	2008-07-13	45.9	S1
NGC 6300				
0037-0850	2003-02-01	2009-10-01	3580	I
0059770101	2001-03-02	2001-03-02	53.2	X1
702049010	2007-10-17	2007-10-18	82.6	S1
10321-01/02	1997-02-14	1997-02-20	26.0	R1
NGC 1142				
0098-0701	2003-08-02	2008-07-11	1629	I
0312190401	2006-01-28	2006-01-28	11.9	X1
701013010	2007-01-23	2007-01-24	101.6	S1
702079010	2007-07-21	2007-07-21	40.6	S2
LEDA 170194				
0028-0768	2003-01-06	2009-01-27	1135	I
0670390301	2012-01-21	2012-01-21	16.9	X1
703007010	2008-12-18	2008-12-20	130.3	S1

APPENDIX C: ISGRI SPECTRA

In Figures C1 and C2 we present the ISGRI spectra of all objects, except for the spectra of NGC 4151, GRS 1734-292, Mrk 509 and NGC 2110, presented in Sec. 3.2. The plotted models correspond to the best-fitting models, listed in Table 3.

This paper has been typeset from a $\text{\TeX}/\text{\LaTeX}$ file prepared by the author.

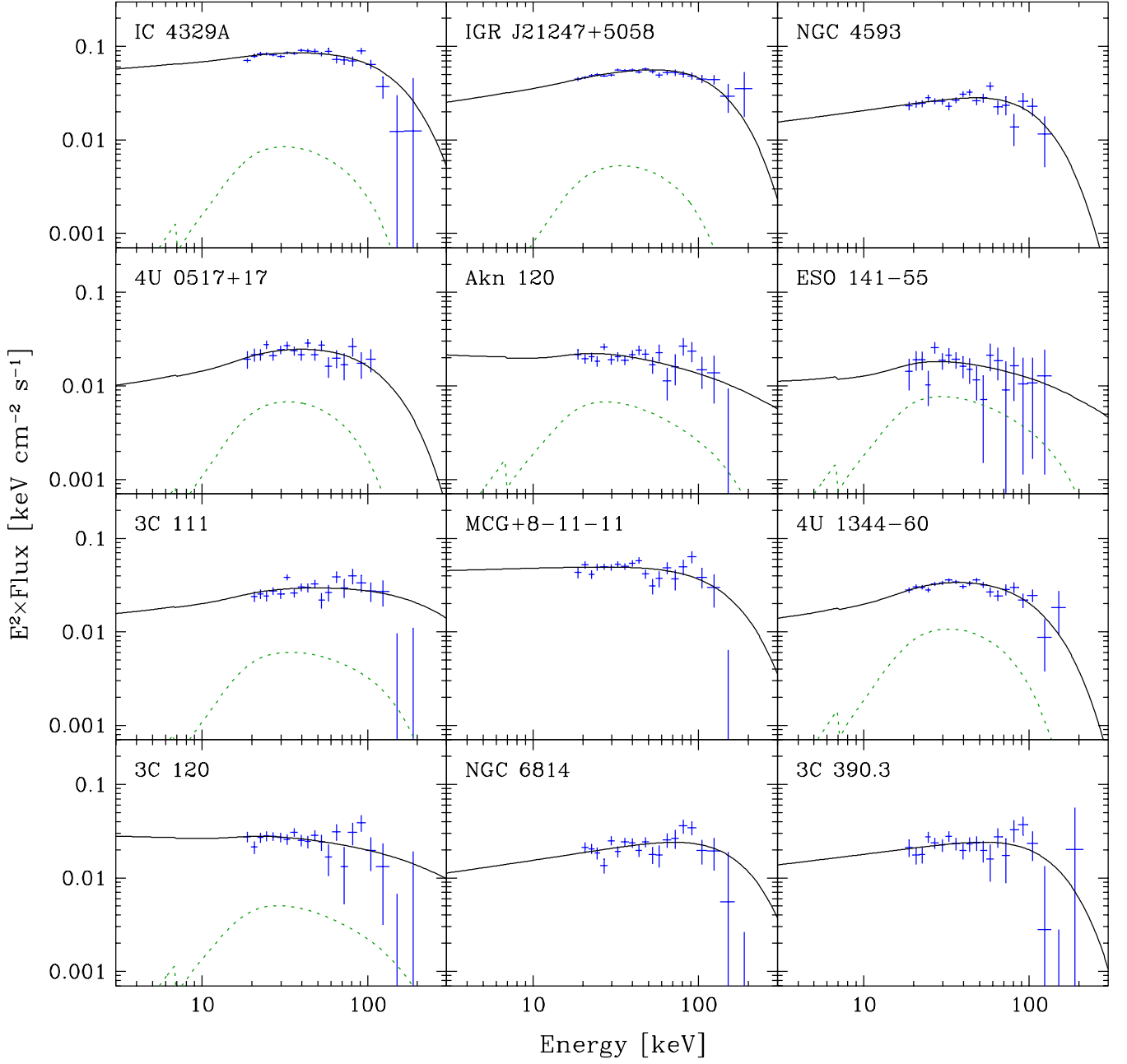


Figure C1. Unfolded ISGRI (blue) spectra of Type 1 and Type 1.5 Seyfert galaxies. Solid line - an unabsorbed Comptonization plus reflection model, dotted line - the reflection component, if present.

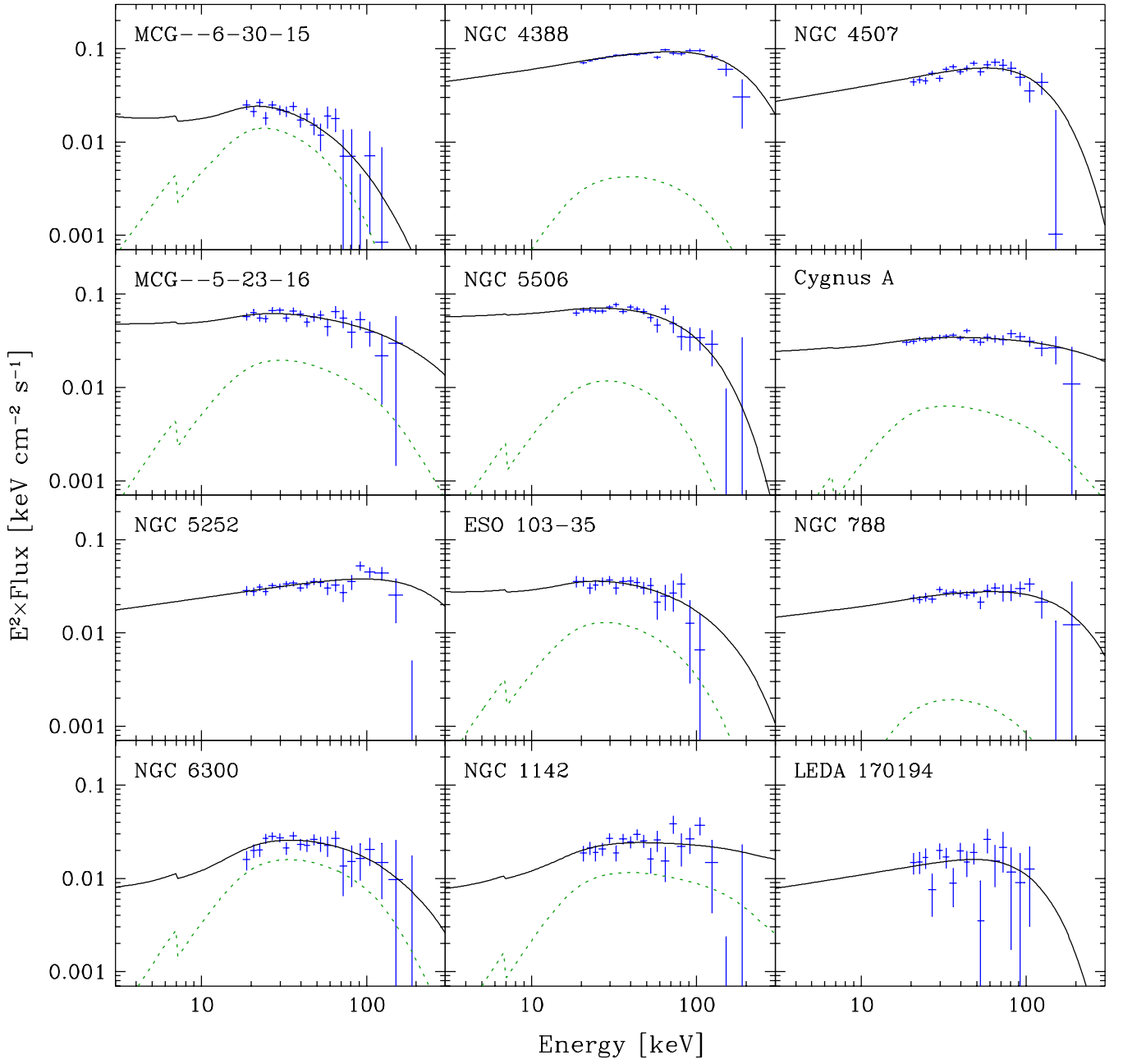


Figure C2. Unfolded ISGRI (blue) spectra of MCG–6-30-15 and Type 2 Seyfert galaxies. Solid line - an unabsorbed Comptonization plus reflection model, dotted line - the reflection component, if present.